

 1918

TALLINNA TEHNIAÜLIKOOL

TALLINN UNIVERSITY OF TECHNOLOGY

Your Thesis Title In English

YOUR NAME

TALLINN 2012

THESIS ON NATURAL AND EXACT SCIENCES BXXX

Your Thesis Title In English

YOUR NAME



TALLINN UNIVERSITY OF TECHNOLOGY

Institute of ...

Laboratory of ...

This dissertation was accepted for the defense of the degree of Doctor of Philosophy (degree name) on Acceptance time.

Supervisor: Your supervisor, PhD
Laboratory of ..., Institute of ...,
Tallinn University of Technology, Tallinn, Estonia

Opponents: Your opponent 1, PhD
Opponent 1 lab/dept.,
Opponent 1 location (university, town, country)

Your opponent 2, PhD
Opponent 2 lab/dept.,
Opponent 1 location (university, town, country)

Defense of the thesis: 23 February 2012

Declaration:

I hereby declare that this doctoral thesis, submitted for the doctoral degree at Tallinn University of Technology, is my original investigation and achievement and has not been submitted for the defense of any academic degree elsewhere.

Your Name

Copyright: Your Name, 2012, Creative Commons Attribution-NonCommercial-NoDerivs 3.0 Unported License

Colophon: This thesis was typeset with $\text{\LaTeX} 2\epsilon$ using André Miede's *classicthesis* style with modifications by David Schryer and Ardo Illaste to conform with Tallinn University of Technology style guidelines. The main font is Libertine (Times compatible). Biolinum is used for sans-serif text.

ISSN 1406-4723

ISBN 978-9949-23-241-3 (publication)

ISBN 978-9949-23-242-0 (PDF)

LOODUS - JA TÄPPISTEADUSED BXXX

Doktoritöö pealkiri eesti keeles

YOUR NAME



CONTENTS

| | |
|---|------|
| SUMMARY | vii |
| KOKKUVÕTE | viii |
| LIST OF PUBLICATIONS | ix |
| LIST OF CONFERENCE PRESENTATIONS | x |
| RELEASED SOFTWARE | xi |
| PREFACE | xii |
| ACKNOWLEDGEMENTS | xiii |
| ACRONYMS | xv |
| | |
| THESIS | 17 |
| 1 INTRODUCTION | 19 |
| 2 RASTER IMAGE CORRELATION SPECTROSCOPY | 23 |
| 2.1 Fundamentals | 23 |
| 2.1.1 Image acquisition | 23 |
| 2.1.2 Correlation function & diffusion | 23 |
| 2.1.3 Time delay between pixels | 27 |
| 2.2 Extensions to RICS | 28 |
| 2.2.1 Motivation for modifications | 28 |
| 2.2.2 Variation of scanning angle | 28 |
| 2.2.3 Variation of scanning resolution | 30 |
| 2.2.4 Two diffusing species | 30 |
| 2.2.5 Triplet states | 31 |
| 2.3 Full form of correlation function | 32 |
| 3 ESTIMATION OF DIFFUSION COEFFICIENTS IN RAT CARDIOMYO- | |
| CYTES | 33 |
| 3.1 Cardiomyocyte preparation | 33 |
| 3.2 Diffusion coefficients in cardiomyocytes | 34 |
| 3.3 Conclusions | 35 |
| 4 NUMERICAL SIMULATIONS OF RESTRICTED DIFFUSION | 39 |
| 4.1 Computational model setup | 39 |
| 4.2 Barrier properties estimated from computational model | 42 |
| 4.3 Conclusions | 42 |
| 5 ONE-DIMENSIONAL COMPUTATIONAL RICS | 45 |

CONTENTS

| | | |
|-----|--|----|
| 5.1 | Motivation & model setup | 45 |
| 5.2 | Barrier effects on regional diffusion coefficients | 45 |
| 5.3 | Conclusions | 47 |
| 6 | HYPERTROPHIC CARDIOMYOPATHY IN RAF1 MUTANTS | 49 |
| 7 | DEVELOPMENT OF CARDIAC ENERGETICS IN POSTNATAL MOUSE HEART | 51 |
| 8 | CONCLUSIONS | 53 |
| | Extended RICS technique | 53 |
| | Estimation of diffusion coefficients of fluorescent dyes | 54 |
| | Mathematical modelling of restricted diffusion | 54 |
| | Cardiomyocyte hypertrophy in Noonan syndrome | 54 |
| | Development of energetic microdomains | 55 |
| | | |
| | BIBLIOGRAPHY | 57 |
| | | |
| | CURRICULUM VITAE | 63 |
| | | |
| | APPENDIX | 67 |
| | | |
| | PUBLICATION I | 69 |
| | | |
| | PUBLICATION II | 73 |
| | | |
| | PUBLICATION III | 77 |

SUMMARY

THIS DISSERTATION EXPLORES the fascinating world of cardiac function and dysfunction. Through application of various experimental and computational techniques new insights into aspects of intracellular diffusion restrictions, causes of hypertrophy, and development of cardiac energetics are gained. Experiments on rat cardiomyocytes using raster image correlation spectroscopy reveal a counterintuitive result, whereby diffusion of a smaller fluorescent molecule is restricted more than that of a larger one, when comparing diffusion in the cytosol to that in solution. A stochastic computational model of diffusion is applied to find a possible explanation for this result. Modeling results suggest the existence of regularly placed semi-permeable barriers in the cardiomyocyte situated $\sim 1 \mu\text{m}$ apart and having very low permeabilities. Such structures in the intracellular environment could enact a significant role in the function of cardiomyocytes, as well as in dysfunctional states of the heart. Also discussed are experiments probing the causes of hypertrophic cardiomyopathy with the aim of studying mutations that affect signalling cascades and cause abnormalities in cardiomyocyte calcium handling.

KOKKUVÕTE

KÄESOLEVAS VÄITEKIRJAS SISENETAKSE südame funktsioneerimise keerulisse aga köitvasse maailma. Rakendades erinevaid eksperimentaalseid ja arvutuslikke meetodeid saadakse uusi teadmisi rakusise diffuseerimisest, südame hüpertroofia ja südameenergeetika arenguliste muutuste valdkondadest. Raster korrelatsioon-spektroskoopia katsed roti südamelihasrakus näitavad, et väiksemate molekulide difusioon on raku sees rohkem takistatud kui suuremate molekulide difusioon. Sellele intuitisoonivastasele tulemusele leitakse seletus kasutades stohastilist arvutuslikku mudelit modelleerimaks rakusisest takistatud diffusiooni. Modelleerimistulemused vihjavad korrapäraste, osaliselt läbitavate barjääride olemasolule südamelihasrakkudes. Nimetatud barjäärid asuksid teine-teisest $\sim 1 \mu\text{m}$ kaugusel ja oleks suhteliselt raskesti läbitavad. Sellised rakusisesed struktuurid võivad omada olulist rolli nii südamelihasrakkude normaalses toimimises kui ka patoloogilistes juhtudes. Antud töö esitab veel katsetulemusi südame hüpertroofia põhjuste uuringuist. Saadud tulemused selgitavad kuidas hüpertroofiat põhjustavad mutatsioonid mõjutavad signaalikaskaade ning põhjustavad ohtlikke kõrvalekaldeid kaltsium-iringluse normaalsest toimimisest südamelihasrakkudes.

LIST OF PUBLICATIONS

- I Illaste A, Kalda M, Schryer DW, Sepp M ; **Life of mice - development of cardiac energetics.** *Journal of Physiology*, 588(23), December 2010
- II Dhandapani P, Fabris F, Tonk R, Illaste A, Karakikes I, Sorourian M, Sheng J, Hajjar R, Tartaglia M, Sobie R, Lebeche D, Gelb B; **Cyclosporine attenuates cardiomyocyte hypertrophy induced by RAF1 mutants in Noonan and LEOPARD syndromes.** *Journal of Molecular and Cellular Cardiology*, Volume 51, Issue 1, July 2011
- III Illaste A, Laasmaa M, Peterson P, Vendelin M; **Analysis of molecular movement reveals latticelike obstructions to diffusion in heart muscle cells.** *Biophysical Journal*, 2012, *in press*

Summary of author's contributions

- I Organizer and main writer for Publication I.
- II For Publication II, which consists of work carried out in Mount Sinai School of Medicine, I carried out some of the confocal microscopy experiments, wrote data analysis software and performed data analysis to ascertain the differences in calcium handling between RAF1-mutation-induced hypertrophic and wildtype cardiomyocytes.
- III In Publication III, consisting of the main results of my doctoral studies, I conducted the raster image correlation spectroscopy (RICS) experiments, improved the design of the experimental protocol, wrote the code for and performed numerical simulations together with analysis of the results, and prepared a large part of the manuscript and figures.

LIST OF CONFERENCE PRESENTATIONS

- I Illaste A, Vendelin M; **Mathematical Model of Mitochondrial Energy Metabolism**; 64th Harden Conference on Mitochondrial Physiology, Ambleside, United Kingdom, September 14 - 18, 2007
- II Illaste A, Vendelin M; **Mathematical Model Of Mitochondrial Energy Metabolism** ; Biophysical Meeting 2008, Long Beach, California, USA, February 2 - 6, 2008
- III Illaste A, Vendelin M; **Computational Model Of Citric Acid Cycle And Oxidative Phosphorylation In Mitochondria**; Biophysical Meeting 2009, Boston, Massachusetts, February 28 - March 4, 2009
- IV Fabris F, Illaste A; Park M; Adler E D; Sobie E A; **Mechanisms Underlying Spontaneous Beating in Human Embryonic Stem Cell-Derived Cardiac Myocytes**; Biophysical Meeting 2010, San Francisco, California, USA, February 20 - 24, 2010
- V Illaste A, Laasmaa M, Schryer D, Birkedal R, Peterson P, Vendelin M; **Determination of Regional Diffusion Coefficients of Fluorescent ATP in Rat Cardiomyocytes**; Biophysical Meeting 2010, San Francisco, California, USA, February 20 - 24, 2010
- VI Illaste A, Laasmaa M, Birkedal R, Peterson P, Vendelin M; **Mapping Diffusion Coefficients of Fluorescent Dyes in Cardiomyocytes**; Biophysical Meeting 2011, Baltimore, Maryland, USA, March 5 - 9, 2011
- VII Illaste A, Laasmaa M, Peterson P, Vendelin M; **Analysis of Molecular Movement Reveals Latticelike Obstructions to Diffusion in Heart Muscle Cells**; Biophysical Meeting 2012, San Diego, California, USA, February 25 - 29, 2012

RELEASED SOFTWARE

LSJuicer – a multi-platform tool for analysing fluorescence vs. time data (e.g., line-scan images from confocal microscopes, csv data from spectrophotometers, fluorimeters, etc). This open-source software was used for analyzing Ca^{2+} transients in Publication II and was also employed for Ca^{2+} spark analysis in [22]. Available at <http://lsjuicer.googlecode.com>

PREFACE

THIS DISSERTATION CONTAINS selected results from my doctoral studies. The main focus of these studies has been on applying RICS for determining properties of diffusion in cardiomyocytes. In the beginning stages of this project an attempt was made to use existing equipment available at Tallinn University of Technology. Unfortunately, after months of trials it became clear that this equipment was not able to carry out the experimental protocol we had developed in a satisfactory manner. As a result of this, we designed and built a confocal microscopy setup of our own, optimized for performing RICS experiments.

Before the building and testing was complete, however, I travelled to New York in order to spend 8 months at Mount Sinai School of Medicine in the laboratory of Dr. Eric A. Sobie. This side-project, although also involving confocal microscopy and cardiac muscle cells, was quite different from what I had previously been involved in. The collaboration developed into an article on hypertrophic cardiomyocytes (Publication II) and resulted in the release of a software package aimed at calcium transient analysis.

On my return to Estonia the work on RICS resumed. Although the technical difficulties with the equipment had now been resolved, optimization of the experimental protocol remained. After a year of fine-tuning and improvements, experiments started to become reproducible. Parallel to conducting experiments, I started working on a stochastic computational model of diffusion that I employed for running RICS simulations *in silico* in order to obtain further insights into the results yielded by biological experiments. The results of this combined approach to study diffusion in cardiomyocytes are presented in Publication III and form the main body of this text.

As RICS is only one method used in our laboratory in its quest to unravel the subtleties of cardiac energetics, it is only suitable that we would monitor other developments in the field. One direct result of this is an article (Publication I) reviewing recent results in postnatal development of energetic microdomains in mouse.

ACKNOWLEDGEMENTS

MY CURIOSITY TOWARDS the world of science got a major boost when my father started purchasing the Scientific American journal in the early nineties so that I could satisfy my appetite for reading about intriguing new aspects of this world. The books that accumulated in my home on topics such as cellular automata, chaos, complexity and fractals captured my attention and kindled my interest in these fascinating fields. I am grateful for his effort in immersing me in these topics and his interest in my ongoing scientific endeavours. The support of my mother for my studies and interests was equally crucial in ensuring that I reach where I am today. I am thankful for the help and guidance from my parents in everything I have undertaken.

During my bachelor studies, after completing a course given by Professor Jüri Engelbrecht, I had the honour of being asked to join the Institute of Cybernetics. Having read his books on chaos and complexity it was a thrill to take one of his classes. It was beyond my wildest dreams, however, to be invited to work on these very same topics I had been reading about and tinkering with on my own just a few years prior. I am thankful to Professor Engelbrecht also for acquainting me with my supervisor Dr. Marko Vendelin, whose enthusiasm and energy accompanied me on my journey into cardiac energetics. Marko's advice and knowledge have made me feel confident when navigating the stormy and unpredictable seas of biophysical research. Also, I will be forever in his debt for introducing me to the most special person in my life.

It has been a pleasure working together with all the members of the Systems Biology lab: the original PhD student gang David, Mari and Mervi with whom we have been through thick and thin, and the latecomers Martin, Niina, Natalja, Jelena, Merle and Päivo. This work would not have been possible without their help. My gratitude also belongs to Dr. Rikke Birkedal for her efforts in ensuring that I have cells to perform experiments on (especially during the do-or-die week during the christmas break in 2011) and to Dr. Pearu Peterson for keeping a watchful eye that the temptation of fuzzy language is fought and that only words based on facts ever get put down on paper.

I am grateful to Dr. Eric A. Sobie from the Mount Sinai School of Medicine for offering me the opportunity to work with him for 8 months in New York and for stepping up to help in a bleak situation caused by unfortunate circumstances.

CONTENTS

Lastly, without the unconditional support and love from my wife Hena, the last years of this journey would have been an immeasurably more arduous undertaking.

Financial support from the Wellcome Trust, the Estonian Science Foundation, as well as the Archimedes Foundation is appreciated.

ACRONYMS

| | |
|-------|---|
| AATP | ATTO633-ATP |
| ADEX | Alexa647-dextran 10K |
| ANT | adenine nucleotide translocase |
| ATP | adenosine triphosphate |
| CF | correlation function |
| CK | creatine kinase |
| CM | cardiomyocyte |
| DC | diffusion coefficient |
| FCS | fluorescence correlation spectroscopy |
| HCM | hypertrophic cardiomyopathy |
| IBS | inter-barrier space |
| ICS | image correlation spectroscopy |
| LSCM | laser scanning confocal microscope |
| NMR | nuclear magnetic resonance |
| PSF | point spread function |
| RAF1 | serine/threonine-protein kinase |
| RICS | raster image correlation spectroscopy |
| ROS | reactive oxygen species |
| SERCA | sarco/endoplasmic reticulum Ca^{2+} ATPase |

THESIS

INTRODUCTION

THE SUBJECTS THAT HAVE BEEN explored during my doctoral studies, employ various methods and approaches. They all, however, deal with the common underlying topic of function and dysfunction of cardiac cells.

The first of these subjects relates to the study of how intracellular compartmentation and diffusion restrictions influence cardiac energetics. The existence of diffusion restrictions has been shown in numerous experiments. For example, studies on caffeine induced tension transients have revealed the restricted access of externally supplied adenosine triphosphate (ATP) to intracellular enzymes consuming ATP [11]. Measurements of O₂ consumption by mitochondria during oxidative phosphorylation in permeabilized cardiomyocytes also indicate existence of diffusion restrictions between mitochondria and extracellular solution [13, 25]. The presence of such compartmentation can be visualized by looking at oscillations of mitochondrial membrane potential induced by reactive oxygen species (ROS) [14] and modulation of the ATP sensitive potassium channel by phosphocreatine [1]. Compartmentation caused by such restrictions and how this affects energy transfer in the heart is a clinically relevant problem [9] and concentrations of molecules involved in intracellular energy transfer can be used as a predictive indicator of mortality in dilated cardiomyopathy patients [19].

Substantial diffusion restrictions have so far been suggested from indirect measurements as mentioned above. In skeletal muscle, nuclear magnetic resonance (NMR) experiments have found diffusion of ATP to be hindered compared to diffusion in water [4, 15]. However, the decrease in diffusion coefficients found in these NMR experiments is not big enough to explain the experimental results from oxygraphy measurements listed above. According to computational modelling attempting to reproduce results from oxygen consumption experiments [24], a decrease several times higher than that found in NMR experiments in the diffusion coefficients of adenine nucleotides is necessary to account for the results from oxygraphy measurements.

Employing a novel fluorescence correlation spectroscopy (FCS) based technique termed raster image correlation spectroscopy (RICS), diffusion of fluorescent ATP

INTRODUCTION

has been measured in cardiac myocytes [29]. The RICS method makes use of the fact that in a confocal image each pixel is separated from another not only in distance but also in time [6, 7]. Combining this knowledge with FCS methods allows one to determine information about molecular dynamics, concentrations and diffusion coefficients from images obtained with most laser scanning confocal microscopes (LSCMs). When applied to estimating the diffusion coefficient (DC) of fluorescently labelled ATP in rat cardiomyocytes [29], a more pronounced reduction was found compared to that determined by NMR. Due to the technical difficulties experienced in [29] the RICS method was extended further and has developed into what forms the main results of this dissertation.

The extended RICS technique developed herein was applied to estimate the DCs of two different fluorescent molecules (ATTO633-ATP and Alexa647-dextran 10K) in rat cardiomyocytes. The results obtained from these measurements were used to determine parameters of hypothesized diffusion restrictions in form of semi-permeable barriers. This was carried out with the aid of a stochastic computational model of restricted diffusion. The extended RICS method was applied in analysis of both, experimental and modelled data. Chapter 2 introduces the RICS method and the fundamentals of the extensions to it that have been employed in this dissertation. It is almost entirely composed of the first chapter of the Supporting Material of Publication III and is included in full to familiarize the reader with the subject. Chapter 3 presents a summary of the experimental results, while Chapter 4 lays out the results obtained from computational model of restricted diffusion. Information presented in Chapters 3 to 4 are concise summaries of the main results given in detail in Publication III and its supporting material. In Chapter 5 some hitherto unpublished aspects concerning computational studies on one-dimensional regional RICS are presented.

The second topic explored in this work concerns hypertrophic cardiomyopathy caused by the Noonan syndrome, which is a relatively common genetic disorder (affecting 1 in 1000-2500 births [5]). It causes abnormal development in many parts of the body and can result in congenital heart defects [20, 27]. Chapter 6 covers results from the experimental study presented in full detail in Publication II, where three common mutations responsible for Noonan syndrome and their effect on downstream signalling pathways are investigated. Methods employed included immunoblotting for determining changes in expression levels of several proteins playing vital roles in Ca^{2+} signalling and confocal fluorescence measurements to establish possible dysfunction of Ca^{2+} handling.

Chapter 7 summarizes the main conclusions from Publication I, where a review of developmental changes in formation of energetic microdomains in cardiomyocytes was presented.

In summary, this dissertation presents a concise overview of the work performed during my doctoral studies. With the exception of Chapter 2, where the details of the extended RICS method have been laid out to introduce the topic to the reader, chapters present only the main results and conclusions from each of the studied topics in order to avoid excessive duplication with respect to the full publications given in the appendix. The reader is invited to consult the appended publications to gain more profound insight into the background information, methods used and physiological implications of the results obtained.

2

RASTER IMAGE CORRELATION SPECTROSCOPY

RASTER IMAGE CORRELATION SPECTROSCOPY is based on merging the concepts of LSCM, FCS and image correlation spectroscopy (ICS)[3, 6]. Detailed reviews are available covering the method and how it relates to other FCS-based methods [7, 10]. Here, a brief overview of the concepts behind RICS and to our modification to this method are presented.

2.1 FUNDAMENTALS

2.1.1 *Image acquisition*

Fundamental to the method of RICS is the realization that in an image obtained by a LSCM, pixels on the image are not only separated in space but also in time [6]. Photons emitted by excited fluorescent molecules are recorded as raster images as the mirrors scan the laser beam on the specimen. When recording a two dimensional raster image, the laser beam moves along one image axis (ξ), spending τ_d seconds acquiring each pixel on the line (dwell time), then flies back to the beginning of the line with flyback time τ_f , moves one pixel forward in the other axis(ψ) and records the second line. This sequential processes is repeated until the whole image has been scanned line by line (Fig. 1), resulting in a rectangular grid of pixels separated in space and time.

2.1.2 *Correlation function & diffusion*

By calculating the correlation function (CF) of the scanned image it is possible to extract information about the space-time relationship between the pixels and to characterize, for example, reaction kinetics, translational and rotational diffusion, conformational dynamics, molecular flow, etc. [7, 10, 16]. This can be done by fitting experimentally obtained CF s with theoretical CF curves derived for the

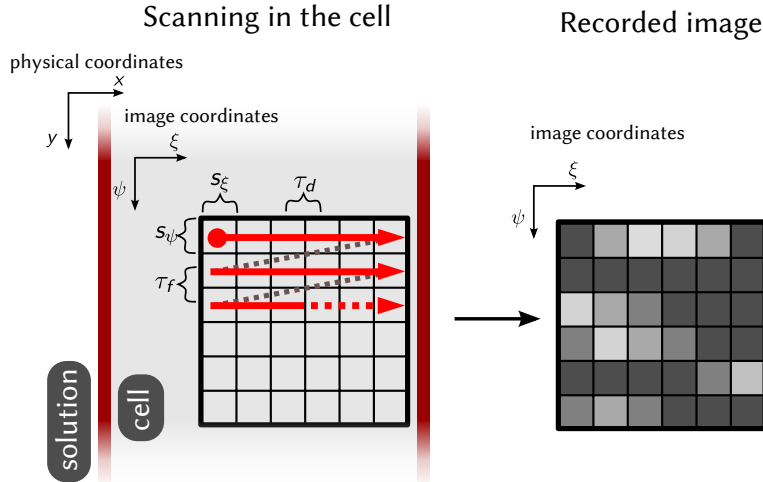


Figure 1 – RICS image acquisition. A raster image consisting of a grid of pixels is acquired within a cell. Pixels are separated by $s_\xi, s_\psi \mu\text{m}$ spatially and by $\tau_d, n_\xi \times \tau_d + \tau_f \mu\text{s}$ temporally in the ξ and ψ directions, respectively. In the default case the image coordinates ξ, ψ align with the physical coordinates x, y . The image obtained (on the right) shows traces of diffusing molecules within the cell.

phenomenon being observed. In this paper we focus on applying RICS on analysis of diffusion of fluorescent dyes.

The correlation function $G(\Delta\xi, \Delta\psi, \Delta\zeta)$ indicates the similarity of an image to a copy of itself shifted by $\Delta\xi$ in the ξ direction, $\Delta\psi$ in the ψ direction (see Fig. 2) and, in case a 3D stack of images is analyzed, $\Delta\zeta$ in the ζ direction (otherwise $\Delta\zeta = 0$).

The CF for a given shift is calculated by multiplying the fluorescence values in the original image with values in the shifted image and averaging over all the pixels. The result is normalized to average image fluorescence squared:

$$G(\Delta\xi, \Delta\psi, \Delta\zeta) = \frac{\langle F(\xi, \psi, \zeta) \cdot F(\xi + \Delta\xi, \psi + \Delta\psi, \zeta + \Delta\zeta) \rangle_{\xi, \psi, \zeta}}{\langle F \rangle_{\xi, \psi, \zeta}^2} - 1, \quad (2.1)$$

where $\langle \dots \rangle$ signifies averaging over the whole image.

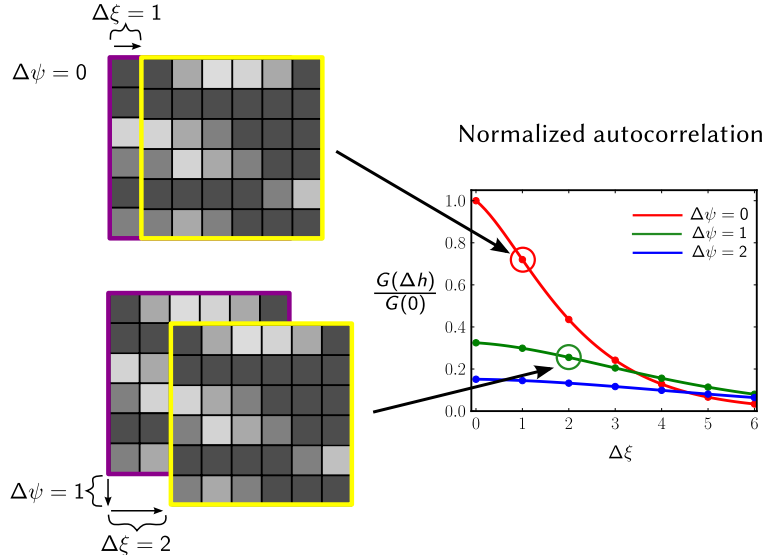


Figure 2 – The correlation function $G(\Delta\mathbf{h})$ for the shift $\Delta\mathbf{h} = (\Delta\xi, \Delta\psi)$ is calculated by shifting a copy of the original image, multiplying the fluorescence values and averaging over the image. Arrows indicate the location of the correlation value for the shifts shown. The CF here is normalized to the zero-shift correlation $G(0)$ from Eq.2.7.

The CF can also be calculated in terms of fluorescence fluctuations from the average $\delta F = F - \langle F \rangle$ by substituting $F = \delta F + \langle F \rangle$ into Eq.2.1:

$$G(\Delta\xi, \Delta\psi, \Delta\zeta) = \frac{\langle \delta F(\xi, \psi, \zeta) \cdot \delta F(\xi + \Delta\xi, \psi + \Delta\psi, \zeta + \Delta\zeta) \rangle_{\xi, \psi, \zeta}}{\langle F \rangle_{\xi, \psi, \zeta}^2}.$$

It is more convenient to present the CF in vector form with image shift vector $\Delta\mathbf{h} = [\Delta\xi, \Delta\psi, \Delta\zeta]$ and position vector $\mathbf{h} = [\xi, \psi, \zeta]$:

$$G(\Delta\mathbf{h}) = \frac{\langle \delta F(\mathbf{h}) \cdot \delta F(\mathbf{h} + \Delta\mathbf{h}) \rangle_{\mathbf{h}}}{\langle F \rangle_{\mathbf{h}}^2}. \quad (2.2)$$

The physical coordinates corresponding to image coordinates \mathbf{h} are $\mathbf{p} = \mathbf{p}_0 + \mathbf{h}\mathbf{S}$. Here, \mathbf{p}_0 is the physical location at the 0-th pixel and $\mathbf{S} = \text{diag}(s_\xi, s_\psi, s_\zeta)$ is a diagonal matrix containing pixel sizes in each image dimension. Shift $\Delta\mathbf{h}$ in image

coordinates converts to a shift $\Delta\mathbf{p} = [\Delta x, \Delta y, \Delta z]$ in the physical coordinate system:

$$\begin{aligned}\Delta\mathbf{p} &= \Delta\mathbf{h}\mathbf{S} = [\Delta\xi, \Delta\psi, \Delta\zeta] \begin{pmatrix} s_\xi & 0 & 0 \\ 0 & s_\psi & 0 \\ 0 & 0 & s_\zeta \end{pmatrix} \\ &= [\Delta\xi \cdot s_\xi, \Delta\psi \cdot s_\psi, \Delta\zeta \cdot s_\zeta] = [\Delta x, \Delta y, \Delta z].\end{aligned}$$

For simplicity we consider that the fluorescence signal recorded at location \mathbf{p} is obtained from the convolution of the point spread function (PSF) of the microscope and the concentration of the fluorescent dye (c) in the PSF volume.

$$F(\mathbf{p}) = B \int W(\mathbf{r}) \cdot c(\mathbf{p} - \mathbf{r}) d\mathbf{r},$$

where W is the PSF and B a parameter called brightness given by $B = q\sigma Q$ [16]. Here, q is the quantum efficiency of detecting emitted photons, σ the cross-section of absorption and Q the emission quantum yield of the fluorescent molecule. Employing this relationship between recorded fluorescence and concentration, Eq.2.2 can be used to connect the fluctuations of fluorescence visible on the recorded image to fluctuations in concentration of the diffusing dye:

$$\begin{aligned}G(\Delta\mathbf{h}) &= \frac{\langle \delta F(\mathbf{p}) \cdot \delta F(\mathbf{p} + \mathbf{q}(\Delta\mathbf{h})) \rangle_{\mathbf{p}}}{\langle F(\mathbf{p}) \rangle_{\mathbf{p}}^2} \\ &= \frac{1}{\langle c(\mathbf{p}) \rangle_{\mathbf{p}}^2} \iint W(\mathbf{r}) W(\mathbf{r}') G_D(\mathbf{r}, \mathbf{r}', \Delta\mathbf{h}) d\mathbf{r} d\mathbf{r}'.\end{aligned}\quad (2.3)$$

G_D is the correlation due to diffusion and can be calculated analytically [28]:

$$\begin{aligned}G_D(\mathbf{r}, \mathbf{r}', \Delta\mathbf{h}) &= \langle \delta c(\mathbf{p} + \mathbf{r}) \cdot \delta c(\mathbf{p} + \mathbf{r}' + \mathbf{q}(\Delta\mathbf{h})) \rangle_{\mathbf{p}} \\ &= \langle c \rangle \prod_{i=1}^n (4\pi D_i)^{-\frac{1}{2}} \exp\left(-\frac{(r'_i + q_i - r_i)^2}{4D_i t(\Delta\mathbf{h})}\right),\end{aligned}\quad (2.4)$$

where $\delta c(\mathbf{p})$ is the fluctuation in concentration of the fluorescent dye at location \mathbf{p} , $\langle c \rangle$ is the average concentration, D_i are diagonal components of the diffusion tensor [4] in the coordinate system composed of principal axes, collected here into $\mathbf{D} = [D_x, D_y, D_z]$. If diffusion is isotropic then all components in \mathbf{D} are equal. In the case of anisotropic diffusion, components of \mathbf{D} can have different values.

The time delay $t(\Delta\mathbf{h})$ indicates how much time has passed between acquisition of two pixels separated by the shift $\Delta\mathbf{h}$. The number n indicates the number of dimensions and in general $n=3$. The equations are still valid, however, for lower n values as well.

Although the PSF is dependent on the microscope and should be measured experimentally, an analytic estimate is often used [16, 28]:

$$W(\mathbf{r}) = \prod_{i=1}^n \exp \left(-2 \frac{r_i^2}{w_i^2} \right) \quad (2.5)$$

Here, \mathbf{w} is a vector describing the width of the PSF in spatial directions. It is customary to perform calibrations using a fluorescent molecule with a known concentration in order to determine the \mathbf{w} values. Furthermore, the x and y components of \mathbf{w} are often assumed to be equal.

Using the PSF definition from Eq.2.5 and G_D from Eq.2.4 the integrals in Eq.2.2 can be calculated and the following analytic form obtained:

$$G(\Delta\mathbf{h}) = \frac{1}{\langle c \rangle} \prod_{i=1}^n \left[\frac{1}{\sqrt{\pi(4D_i t(\Delta\mathbf{h}) + w_i^2)}} \exp \left(-\frac{q(\Delta\mathbf{h})_i^2}{4D_i t(\Delta\mathbf{h}) + w_i^2} \right) \right]. \quad (2.6)$$

From this result it can be seen that with zero shift (i.e., $\Delta\mathbf{h} = (0, 0, 0)$) the CF gives:

$$G(0) = \frac{1}{\langle c \rangle} \prod_{i=1}^n \frac{1}{\sqrt{\pi} w_i}. \quad (2.7)$$

As $G(0)$ is independent of the diffusion of the fluorescent molecule it can be used to determine the global concentration of the molecule or, knowing that, the properties of the PSF (i.e., components of \mathbf{w}).

2.1.3 Time delay between pixels

Scanning a 2D raster image with n_ξ pixels in the ξ direction, with τ_d seconds used as the dwell time for all pixels and τ_f being the time that it takes for the beam to move from the end of one line to the beginning of the next, the time delay between two pixels separated by the shift $\Delta\mathbf{h}$ used in Eqs. 2.6 and 2.9 is:

$$t(\Delta\mathbf{h}) = t(\Delta\xi, \Delta\psi) = \Delta\xi \cdot \tau_d + \Delta\psi \cdot (n_\xi \cdot \tau_d + \tau_f). \quad (2.8)$$

Inserting this relation in the CF Eqs. 2.6 and 2.9 will yield the function that can be used for fitting experimentally obtained data and obtaining diffusion coefficients.

2.2 EXTENSIONS TO RICS

2.2.1 Motivation for modifications

As we have demonstrated, RICS can be used to determine anisotropy of diffusion by varying the time delay between physical location in the sample during a scan. This can be achieved by altering the angle of scanning [29].

Also, diffusion dependent changes in the CF can be subtle, making them hard to detect and fit, especially with noisy data. Through changes in scanning resolution additional aspects of the CF can be estimated, leading to a larger amount of datapoints available for fitting.

2.2.2 Variation of scanning angle

In order to detect anisotropy of diffusion, several scanning angles can be used to alter the time delay between pixels acquired from the same location [29]. When scanning is performed at an angle α relative to the physical coordinate axes, the

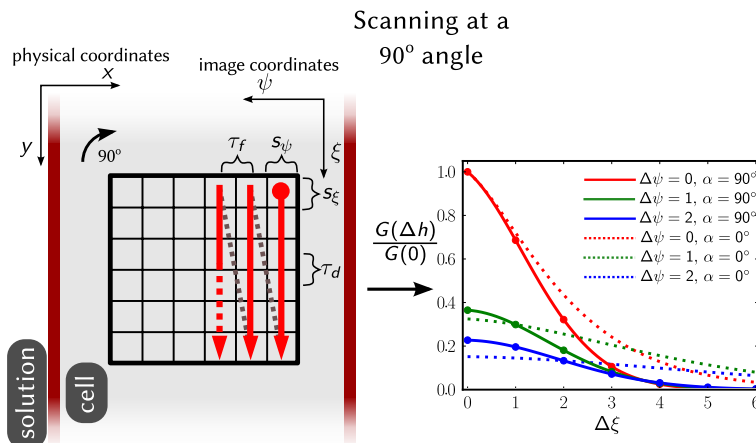


Figure 3 – Modified scanning for RICS. Scanning at an angle α rotates the image coordinates with respect to the physical coordinates and results in a different CF which can be used for determining anisotropy of diffusion. The CF for 0° angle scanning from Fig. 2 is shown in dotted lines and differs from the CF obtained for an image scanned at a different angle. In the shown example, scanning is performed at a 90° angle, effectively aligning the image ξ axis with the physical y axis and image ψ axis with physical x axis.

CF equations need to be modified to account for this. For example, if scanning is performed under a 90° angle, the image ξ and ψ axes actually correspond to the physical y and x axes, respectively (see Fig. 3). The CF that takes the scanning angle into account is:

$$G(\Delta\mathbf{h}, \alpha) = \frac{1}{\langle c \rangle} \prod_{i=1}^n \left[\frac{1}{\sqrt{\pi(4D_i t(\Delta\mathbf{h}) + w_i^2)}} \exp\left(-\frac{q(\Delta\mathbf{h}, \alpha)_i^2}{4D_i t(\Delta\mathbf{h}) + w_i^2}\right) \right], \quad (2.9)$$

where the physical shift $\Delta\mathbf{p}$ is now a function of the rotation angle α :

$$\Delta\mathbf{p}(\Delta\mathbf{h}, \alpha) = \Delta\mathbf{h} \mathbf{S}(\mathbf{M}(\alpha))^T \quad (2.10)$$

$\mathbf{M}(\alpha)$ is the rotation matrix for rotation angle α . For rotating around the z axis, as is done in this paper, the rotation matrix is:

$$\mathbf{M}(\alpha) = \begin{pmatrix} \cos \alpha & -\sin \alpha & 0 \\ \sin \alpha & \cos \alpha & 0 \\ 0 & 0 & 1 \end{pmatrix}.$$

It is possible to do rotations around another axis or even multiple rotations around different axes by inserting a suitable rotation matrix in Eq.2.10 (assuming that the microscope employed is able to perform such scans).

The physical shift vector from Eq.2.10 for rotation α around the z axis is:

$$\begin{aligned} \Delta\mathbf{p}(\Delta\mathbf{h}, \alpha) &= [\Delta x, \Delta y, \Delta z] \\ &= \Delta\mathbf{h} \mathbf{S}(\mathbf{M}(\alpha))^T \\ &= \begin{pmatrix} \Delta\xi \cdot s_\xi \\ \Delta\psi \cdot s_\psi \\ \Delta\zeta \cdot s_\zeta \end{pmatrix}^T \begin{pmatrix} \cos \alpha & \sin \alpha & 0 \\ -\sin \alpha & \cos \alpha & 0 \\ 0 & 0 & 1 \end{pmatrix} \\ &= \begin{pmatrix} \Delta\xi \cdot s_\xi \cdot \cos \alpha - \Delta\psi \cdot s_\psi \cdot \sin \alpha \\ \Delta\xi \cdot s_\xi \cdot \sin \alpha + \Delta\psi \cdot s_\psi \cdot \cos \alpha \\ \Delta\zeta \cdot s_\zeta \end{pmatrix}^T. \end{aligned}$$

It is easy to verify that when $\alpha = 0$, \mathbf{M} reduces to the identity matrix and Eq.2.9 simplifies to Eq.2.6.

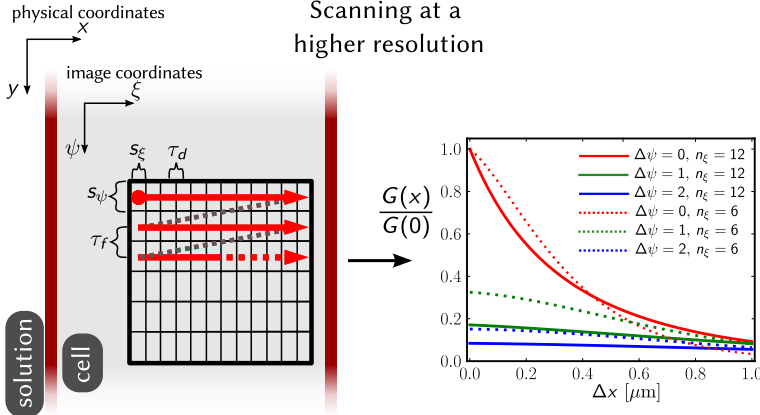


Figure 4 – Modified scanning for RICS. Changing the scanning resolution also alters the shape of the CF. In the example shown, the image is scanned at two times higher resolution resulting in the CF depicted with solid lines. Since the pixel dwell time τ_d is not changed, scanning one line takes two times longer. For comparison, the CF from Fig. 2 is shown in dotted lines. The horizontal axis now shows physical shift values in μm since the pixel size and count for the two CFs is different.

2.2.3 Variation of scanning resolution

Changes in scanning resolution [29] or pixel dwell time τ_d [8] will alter the time delay function Eq.2.8 and result in different correlation curves. An example for scanning with double resolution but unchanged pixel dwell time τ_d in ξ axis is shown on Fig. 4. An increased resolution increases the time taken to record a line and decreases pixel size. Therefore, in order to compare the CF for different resolutions it is more suitable to present them as functions of physical distance as is done in Fig. 4.

2.2.4 Two diffusing species

It is possible for the fluorescent molecule to bind with other, larger, molecules in the intracellular solution. As a result, two subspecies of the fluorescent molecule would be diffusing in the cell: the faster unbound form and the slower bound form. Assuming that fluorescent properties of the dye are not altered as a result of

binding and that the two species are non-interacting (i.e., the binding/unbinding is relatively slow), the CF for two species diffusing is [12, 16] :

$$G(\Delta\mathbf{h}, \alpha) = \frac{1}{\langle c_1(\mathbf{p}) + c_2(\mathbf{p}) \rangle_{\mathbf{p}}^2} \cdot \iint W(\mathbf{r})W(\mathbf{r}') (\langle c_1 \rangle \cdot g_{D1} + \langle c_2 \rangle \cdot g_{D2}) d\mathbf{r} d\mathbf{r}', \quad (2.11)$$

where $\langle c_1 \rangle, \langle c_2 \rangle$ are concentrations of the two components and g_{D1} and g_{D2} are given by $G_{Dk}(\mathbf{r}, \mathbf{r}', \Delta\mathbf{h}, \alpha)/\langle c_k \rangle$, ($k = 1, 2$). Inserting the gaussian PSF given in Eq.2.5 to calculate the CF for two components from Eq.2.11:

$$G(\Delta\mathbf{h}, \alpha) = \frac{1}{(\langle c_1 \rangle + \langle c_2 \rangle)^2} \cdot \left[\langle c_1 \rangle \prod_{i=1}^n \frac{\exp\left(-\frac{q(\Delta\mathbf{h}, \alpha)_i^2}{4D_{1,i}t(\Delta\mathbf{h})+w_i^2}\right)}{\sqrt{\pi(4D_{1,i}t(\Delta\mathbf{h})+w_i^2)}} + \langle c_2 \rangle \prod_{i=1}^n \frac{\exp\left(-\frac{q(\Delta\mathbf{h}, \alpha)_i^2}{4D_{2,i}t(\Delta\mathbf{h})+w_i^2}\right)}{\sqrt{\pi(4D_{2,i}t(\Delta\mathbf{h})+w_i^2)}} \right],$$

where $D_{1,i}, D_{2,i}$ are diffusion coefficients in direction i for the first and second component, respectively.

2.2.5 Triplet states

It is possible for a fluorescent molecule to go into a so-called triplet state from where it relaxes back to ground state after a delay much longer than it takes for the normal excitation-emission cycle to complete. This phenomenon, if ignored, could cause diffusion coefficients to be overestimated. To account for this effect, we multiply the CF function (Eq.2.9 or Eq.2.11) with a compensation factor [8, 10, 12, 31] :

$$1 + \frac{T}{1-T} \exp\left(-\frac{t}{\tau}\right), \quad (2.12)$$

where T is the fraction of molecules in triplet state and τ the triplet state relaxation time.

2.3 FULL FORM OF CORRELATION FUNCTION

In this work the experimentally measured PSF was used instead of the approximated one (Eq.2.5), necessitating numerical integration for each CF evaluation:

$$G(\Delta h, \alpha) = \frac{1}{\langle F_1(p) + F_2(p) \rangle_p^2} \left(1 + \frac{T}{1-T} \exp\left(-\frac{t}{\tau}\right) \right) \cdot \iint W(r)W(r') (\langle c_1 \rangle \cdot g_{D1} + \langle c_2 \rangle \cdot g_{D2}) dr dr' \quad (2.13)$$

This is the CF form used for fitting experimental data in this work.

3

ESTIMATION OF DIFFUSION COEFFICIENTS IN RAT CARDIOMYOCYTES

3.1 CARDIOMYOCYTE PREPARATION

N EITHER OF THE DYES USED in this work (ATTO633-ATP and Alexa647-dextran 10K) are able to permeate the cell membrane. This can be seen on Fig.5, where, contrary to the fluorescent signal from the membrane permeable form of Mitotracker Green dye (Fig.5A), ATTO633-ATP is not able to pass into the cytosol (Fig.5B). In order to use RICS to estimate the DCs of these dyes, they have to be allowed to enter into the cell. This can be achieved through saponin permeabilization of the cell membrane [29]. Initially, saponin permeabilization was used also in this work, but it became evident that exposure to saponin resulted in the cells hypercontracting within a few hours. The full protocol for RICS measurements, however, takes several hours to complete. This necessitated the need to come up with an alternative method of introducing the dyes into the cell.

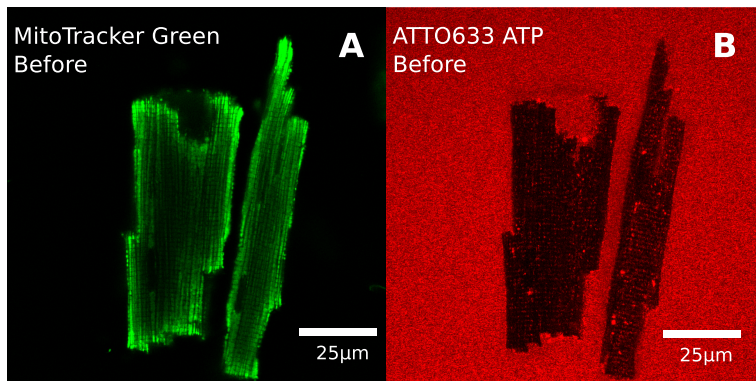


Figure 5 – Confocal images of rat cardiomyocytes in measurement solution. On the left image (A) membrane permeable Mitotracker Green dye has permeated the membrane and accumulates in the cell. On the right image (B) ATTO633-ATP is visible in the solution outside the cell and is not able to enter the cytosol.

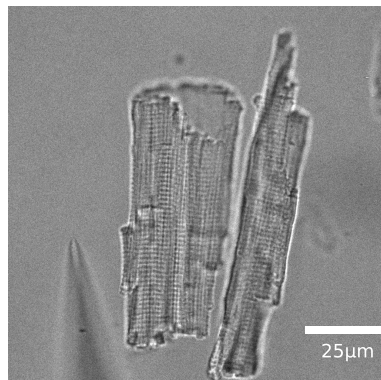


Figure 6 – The cell membrane is permeated mechanically with a glass pipette (tip $\varnothing 0.5 \mu\text{m}$). Both the pipette and the cell are shown on this transmission image.

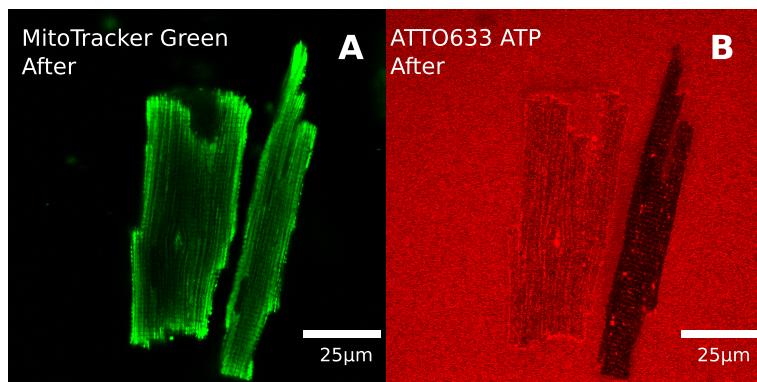


Figure 7 – Confocal images of cardiomyocytes after “poking”. The Mitotracker Green signal is unaltered (A) but fluorescence from ATTO633-ATP is now visible in the cytosol.

In this work, viable permeabilized cells were obtained by using a glass pipette with a diameter of 0.5 μm to mechanically “poke” 2-3 holes into the cell membrane (Fig.5). Within minutes after completing this procedure, fluorescence signal from ATTO633-ATP could be recorded from within the cell. After this the full RICS protocol was carried out. Compared to saponin permeabilization, the viability of the “poked” cells was increased by several hours.

3.2 DIFFUSION COEFFICIENTS IN CARDIOMYOCYTES

Diffusion coefficient estimates were obtained by fitting the experimentally calculated CF with the theoretical CF from Eq.2.13 as explained in detail in Publication III. A summary of the results obtained is presented in Table 1. The table with full experimental results is given in Publication III. The two DCs shown for ATTO633-

3.3 CONCLUSIONS

| Dye | Media | Cmp. | Diffusion | |
|---------------------|----------|------|--------------------------------------|-----------------------------------|
| | | | D_{TR} $\mu\text{m}^2/\text{s}$ | D_L $\mu\text{m}^2/\text{s}$ |
| ATTO633-ATP | water | | 326±13 | |
| | solution | | 195±8 | |
| | CM | 1 | 0.7±0.3 | 0.8±0.2 |
| | | 2 | 24±6 | 35±8 |
| Alexa647-dextran10K | water | | 62±1 | |
| | solution | | 53±1 | |
| | CM | | 16±2 | 19±3 |
| | | | | |
| ATTO655-COOH | water | | 454±3 | |

Table 1 – Diffusion coefficient values for ATTO633-ATP and Alexa647-dextran 10K in water, solution and cardiomyocyte. In case of anisotropic diffusion, DC values for both transverse(TR) and longitudinal(L) directions are given (DC in the z direction is assumed equal to the DC in x direction). For isotropic diffusion only one DC is shown which applies for all directions. Data shown is mean ± standard deviation.

ATP in cardiomyocyte (CM) are the slow and freely diffusing forms of the dye. Separating ATTO633-ATP into two subspecies was necessary due to ATTO633-ATP probably binding to some intracellular proteins and thereby creating a second, slower diffusing form of ATTO633-ATP. For Alexa647-dextran 10K a second component was not necessary.

Also shown, are results for a third dye (Atto655-COOH) diffusing in water. The DC of this dye has been determined in water [17], allowing us to use this data to test the accuracy of our method. Our estimate of 454±3 $\mu\text{m}^2/\text{s}$ obtained at 26° is in good agreement with published data for Atto655-COOH: 426±6 $\mu\text{m}^2/\text{s}$ obtained at 25° [17] after correcting for the temperature difference.

On Fig.8 results for ATTO633-ATP and Alexa647-dextran 10K are presented graphically. From here the effect of anisotropy of diffusion and the reduction experienced by ATTO633-ATP and Alexa647-dextran 10K can be seen.

3.3 CONCLUSIONS

The most striking result of this study is the fact that the DC of ATTO633-ATP is reduced more than that of Alexa647-dextran 10K when comparing diffusion in CM

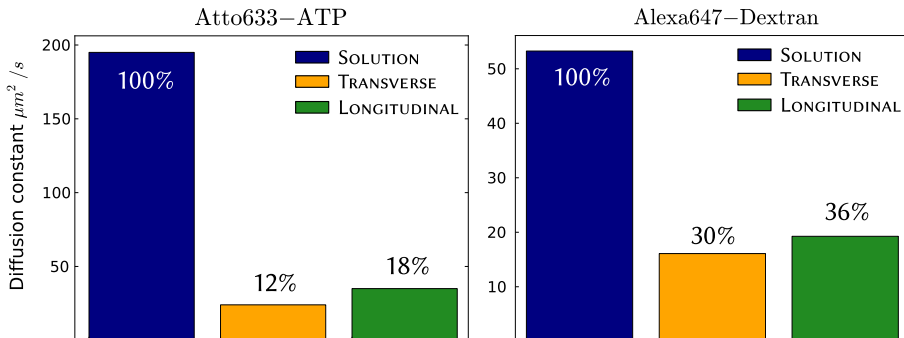


Figure 8 – Diffusion coefficients of ATTO633-ATP and Alexa647-dextran 10K in solution and cardiomyocyte. The percentages show the DCs relative to DC in solution.

and solution. This is visualized in Fig.9 where the ratio of DC of ATTO633-ATP to that of Alexa647-dextran 10K is shown. As can be seen, the more than 3 time difference in solution is reduced to less than 2 in the cytoplasm, indicating that the diffusion of the smaller molecule (ATTO633-ATP) is hindered more than that of the larger one (Alexa647-dextran 10K). This is unexpected, as relative decrease of DC is usually larger for larger molecules [18].

Secondly, longer viability of the cardiomyocytes during the duration of the experimental protocol indicates that the employed “poking” technique is a good alternative to saponin permeabilization. The drawback of the method is that it is time consuming and requires more specialized equipment than is needed when using saponin permeabilization. Furthermore, depending on how well the cells attach to the laminin coated coverslip, several cells might need to be poked before the procedure is successful and a permeated CM is obtained for performing RICS measurements. A different approach of localized permeabilization can be used as

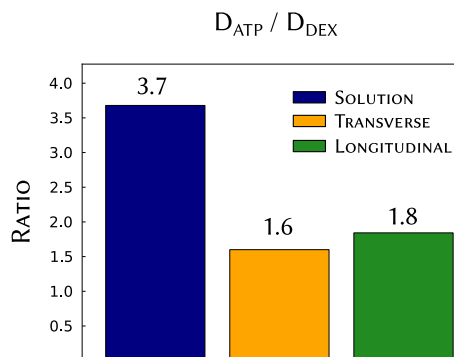


Figure 9 – Ratio of DCs of ATTO633-ATP and Alexa647-dextran 10K in solution and in the transverse and longitudinal directions of the cell.

well. In this approach saponin is applied locally by a micropipette in only one region of the cardiomyocyte [1], whereby only a section of the cell is exposed and permeabilized. However, this would require extra equipment in addition to that used in the “poking” procedure.

Lastly, increasing the amount of physical phenomena taken into account when deriving the theoretical correlation function increases the ability of the theoretical fit to match experimental data. Addition of anisotropic diffusion, two diffusing components of the same dye and triplet state dynamics to the CF as demonstrated in Chapter 2 increases the ability to produce consistent DC estimations. Naturally, care has to be taken to avoid overparameterizing the theoretical model used for fitting experimental data. Additions to the theoretical CF are made only in cases when the physical process being observed warrants it. For example, when fitting Alexa647-dextran 10K data from cardiomyocytes, a single component model is used instead of a two component one, since the underlying physical process is deduced to be of only one species of Alexa647-dextran 10K diffusing.

4

NUMERICAL SIMULATIONS OF RESTRICTED DIFFUSION

IN GENERAL, THE DIFFUSION COEFFICIENT of a smaller molecule is reduced less during the transition from solution to the cytosol than the DC of a larger molecule [26]. For example, if we consider the diffusion restrictions imposed by actomyosin, then the larger molecule, such as Alexa647-dextran 10K, would not be able to pass through some of the openings in the spatial structure which are traversable to smaller molecules such as ATTO633-ATP. This would results, predictably, in the DC of Alexa647-dextran 10K being reduced more in the cytosol than ATTO633-ATP. However, as can seen from our experimental results from Chapter 3, the DC of the smaller molecule is reduced more in transition from solution to CM cytosol compared to the larger molecule. As shown by earlier modelling studies of respiration kinetics, diffusion in CMs could be restricted by local barriers [23, 30]. We explored this possibility by testing whether simple planar permeable barriers could restrict diffusion of fluorescent dyes to the extend established from experiments shown in Chapter 3.

4.1 COMPUTATIONAL MODEL SETUP

A stochastic computational model of diffusion was used to perform RICS experiments *in silico*.

Full details of the mathematical model are presented in Publication III. In short, the model consisted of a lattice of permeable barriers separated from each other by a certain distance (as depicted on Fig.10). Fluorescent dye molecules diffuse in the inter-barrier space (IBS) with a DC that is reduced compared to the DC in solution by a factor λ (i.e., $DC_{IBS} = \lambda \cdot DC_{solution}$). Barrier permeability (resulting from η pores of radius R nm per μm^2 of barrier area) and barrier-to-barrier distance (d), as well as the reduction of the DC in the inter barrier space (λ) were parameters which were estimated with the aid of the computational model. Parameters were allowed to be different in different spatial directions (longitudinal - L and transverse - TR).

Together with simulating stochastic diffusion, the model generated images similar to those obtained from confocal microscopy experiments. RICS analysis was applied to these images and apparent DCs estimated. The apparent DC determined by RICS is the result of molecules diffusing in the inter-barrier space and interacting with the permeable barriers. A collection of apparent ATTO633-ATP DCs obtained from modelling are presented in Fig.11A. The dependence of the apparent DC estimated from the model is plotted as a function of barrier-to-barrier distance for various barrier permeability values. It can be seen that as barrier permeability increases, the effect of the barriers on the apparent DC decreases. Since the actual DC was estimated from experiments on cardiomyocytes as presented in Chapter 3, it is possible to find at which barrier-to-barrier distance and barrier permeability values the model produces the same apparent DC as the experiment. It is helpful to explain the procedure in terms of intersections on plots in parameter space. For this, the experimentally estimated DC is plotted on the graph of model results (the horizontal line D_{TR}^{exp} in Fig.11A). At points where model result curves and the line representing the experimental value intersect, the model yields the experimentally obtained DC. For clarity the intersection region is magnified in the inset

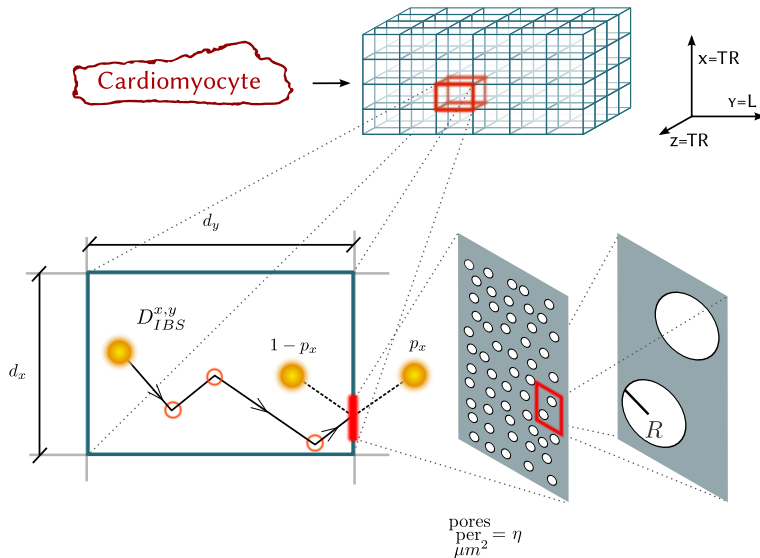


Figure 10 – Scheme of the computational model. Intracellular structure of the cell (top left) is approximated by a 3D lattice of barriers which hinder molecule diffusion (top right). Barriers are placed, depending on direction α , d_α μm apart and have permeabilities p_α . Diffusion coefficient in the space between barriers is reduced by a factor λ compared to solution ($0 < \lambda \leq 1$). Stochastically diffusing molecules interact with barriers and have a probability p_α of passing through (bottom left). Permeable barriers correspond to porous walls with η pores of radius R per μm^2 of barrier area (bottom right). Apparent diffusion coefficients are estimated over the entire lattice by employing RICS analysis on images acquired from the model.

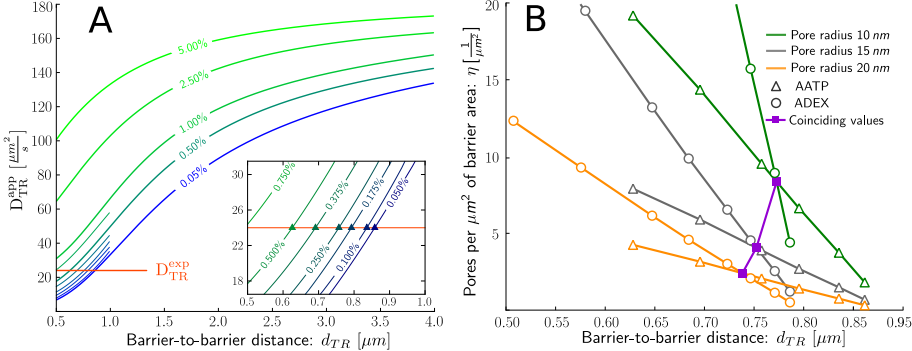


Figure 11 – (A) Apparent diffusion constant values for ATTO633-ATP are obtained from simulations with varying barrier distances (horizontal axis) and permeabilities (indicated by values on curves). Horizontal solid line shows ATTO633-ATP diffusion coefficient estimated from experiment ($D_{\text{TR}}^{\text{exp}}$). Inset covers the region $0.5 \dots 1 \mu\text{m}$ where curves intersect with experimental data. Intersection points are marked with triangles. (B) Points of intersection from A with permeability converted to pores per μm^2 for different pore radius values (10, 15 and 20 nm). Intersections of ATTO633-ATP (\triangle) and Alexa647-dextran 10K (\circ) curves of identical pore radius values signify points where model and experiment coincide for both molecules simultaneously (■). Intersections are curves in 3D space (barrier-to-barrier distance vs. pore radius vs. pores per μm^2).

of Fig.11A. The same procedure is performed for Alexa647-dextran 10K with the experimentally determined DC of Alexa647-dextran 10K in CM used for finding intersections.

As a result of this we obtain a set of barrier-to-barrier, permeability value pairs for both ATTO633-ATP and Alexa647-dextran 10K at which the computational model of restricted diffusion yields experimentally obtained DCs. As explained in Publication III, barrier permeability values for ATTO633-ATP and Alexa647-dextran 10K are not directly comparable. It is possible, however, to convert from barrier permeability to the number of pores per unit barrier area (η) by fixing a certain pore radius (R). These two parameters are independent of the diffusing dye, allowing the model parameter values obtained for ATTO633-ATP and Alexa647-dextran 10K to be compared. This is done by plotting them together for different pore radius values (Fig.11B). At points where ATTO633-ATP and Alexa647-dextran 10K curves intersect, the computational model is able to reproduce the experimentally estimated DCs for both ATTO633-ATP and Alexa647-dextran 10K simultaneously. From Fig.11B it is possible to establish the range of parameters (d , η , R) at which the model is able to match results from experiments on cardiomyocytes.

| Model parameter | Direction | | | |
|---|-----------------|-----------------|-----------------|-----------------|
| | transverse | | longitudinal | |
| | TR (x,z) | min | max | L (y) |
| Distance d [μm] | 0.68 ± 0.10 | 0.87 ± 0.07 | 0.73 ± 0.13 | 1.02 ± 0.10 |
| Pore radius R [nm] | 7.4 ± 2.1 | 30 ± 8 | 6.7 ± 1.8 | 38 ± 10 |
| Pore density η [$1/\mu\text{m}^2$] | 1.2 ± 0.1 | 29 ± 23 | 1.1 ± 0.1 | 48 ± 37 |
| λ_{AATP} | 0.78 ± 0.13 | 1.0 | 0.78 ± 0.13 | 1.0 |
| λ_{ADEX} | 0.77 ± 0.14 | 1.0 | 0.77 ± 0.14 | 1.0 |

Table 2 – Properties of barriers restricting diffusion predicted by stochastic model on the basis of RICS measurements. Data presented is mean \pm standard deviation.

4.2 BARRIER PROPERTIES ESTIMATED FROM COMPUTATIONAL MODEL

The ranges collected from intersections in Fig.11B represent parameter values where both ATTO633-ATP and Alexa647-dextran 10K are able to simultaneously match experimental DCs and are presented as the results from the computational model in Table 2. In general, barriers need to be spaced $\sim 1 \mu\text{m}$ from each other, have a small number of nanometer scale pores, and the DC in the inter-barrier should be comparable to DC in solution in order for the model to reproduce experimental results.

Errors for the model parameters were estimated by Monte Carlo simulation outlined in the Supporting Material of Publication III. Since the minimal and maximal values of some of the parameters do not follow a normal distribution, the mean and standard deviation values are less informative than the shape of the actual distribution for which the Supporting Material of Publication III should be consulted.

4.3 CONCLUSIONS

The stochastic model for simulating restricted diffusion with regular permeable barriers can match experimentally found DCs for ATTO633-ATP and Alexa647-dextran 10K in the case when:

- barriers in the model are located relatively close to each other ($<1 \mu\text{m}$ apart)

- permeability of these barriers is relatively low (containing $\sim 1\dots40$ pores of radius $7\dots30$ nm per μm^2)
- the DC in the inter-barrier space is lower than that of diffusion in solution by a factor $0.8\dots1$.

Diffusional anisotropy results in the ranges of the parameters differing slightly in different spatial directions as visible from Table 2.

The choice of model geometry employed here, whereby regularly placed semi-permeable barriers cause restrictions to diffusion, is not the only geometry that can explain the paradoxical result where a smaller molecule is restricted more than a larger one. Our model setup was motivated by its relative simplicity compared to more complex geometries. Although already this simple geometry was able to give an answer to the raised question, more complicated model geometries with sub-volumes excluding the larger dye could be explored in the future.

5

ONE-DIMENSIONAL COMPUTATIONAL RICS

ACCORDING TO OUR ANALYSIS, profound barriers to diffusion exist in cardiomyocytes. To test whether it is possible to localize such diffusion obstacles in RICS measurements we again turned to mathematical modelling.

5.1 MOTIVATION & MODEL SETUP

So far in this dissertation, RICS analysis has been performed and DCs estimated from the entire region acquired in either experiment or computational model. Here, a different approach is used. One-dimensional RICS simulations are performed as previously (see Chapter 4 and Publication III). Two barrier-to-barrier distances (5 and 1 μm) and several barrier permeabilities (p) ranging from 0 to 75% are used as model parameters. Molecules diffuse in the inter-barrier space with a given DC (D_{IBS}) in one dimension. When coming in contact with a barrier they can either pass through the barrier or bounce back. The probability of doing either is determined by the permeability of the barrier. The computational model produces linescan images of a 20 μm region. In subsequent processing the region is divided into smaller subregions and RICS analysis is performed on each of these independently and apparent DCs found (D_{app}). For comparison, analysis on the whole 20 μm region is performed also, similarly to the analysis in Chapter 4.

5.2 BARRIER EFFECTS ON REGIONAL DIFFUSION COEFFICIENTS

From performing the regional analysis described above, a sequence of DCs can be obtained. An example of simulation and regional analysis results is presented on Fig. 12. Here, the DC in the IBS is set to $D_{IBS} = 40 \mu\text{m}^2/\text{s}$ and within the 20 μm space there are 4 barriers restricting diffusion, placed at 5 μm from each other. The permeabilities of these barriers are varied in order to study the effect of permeability on the estimated apparent DCs obtained from RICS analysis. Results obtained for a range of barrier permeability values are represented by different curves in

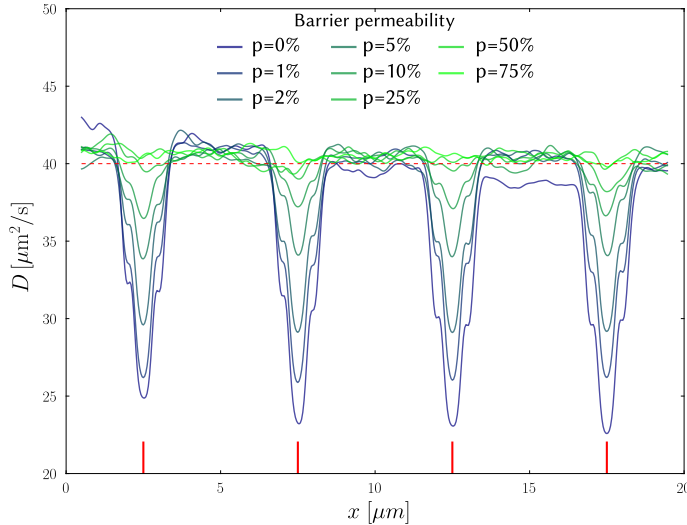


Figure 12 – DCs obtained from regional RICS analysis of linescan data obtained from a computational model. Barriers (indicated by short vertical lines) are places 5 μm apart and their permeability(p) is varied between model runs. DCs obtained for varying permeability values are shown with different lines. The value shown at any x location is the DC obtained from RICS analysis on the 1 μm segment centered at that location.

Fig. 12. It is visible that the apparent DC reduces almost twofold in regions with a barrier in the center.

The relative decrease in DC ($\Delta D/D_{IBS} = (D_{IBS} - D_{APP})/D_{IBS}$), calculated for the region around a single barrier is averaged for equivalent neighbourhoods around each barrier and the curves shown in Fig. 13A are obtained. The solid horizontal line indicates the position of the barrier, dashed lines show the 5 μm region centered at the barrier. It can be seen from the plot that even in cases when the region used for RICS estimation does not include the barrier (i.e., any point outside of the dashed lines), the barrier still affects the DC.

A similar analysis for a model with barriers separated by 1 μm is shown on Fig. 13B. In this case the region used for RICS analysis is limited to 1 μm but is plotted on the same scale as Fig. 13A to make comparison easier. Compared to the 5 μm barrier distances on Fig. 13A, the presence of more closely placed barriers causes a decrease in the apparent DC further away from the barrier.

When the maximum relative decrease of DC relative to the DC in IBS is calculated as a function of permeability, the effect of the region size used for DC estimation in RICS becomes visible. On Fig. 14 curves showing the maximum relative decrease for 3 different region sizes are plotted. From here it can be seen that as the region size increases the effect barriers have on the apparent DC is lessened. When the whole image is analysed as a single 20 μm region, the decrease in DC is

5.3 CONCLUSIONS

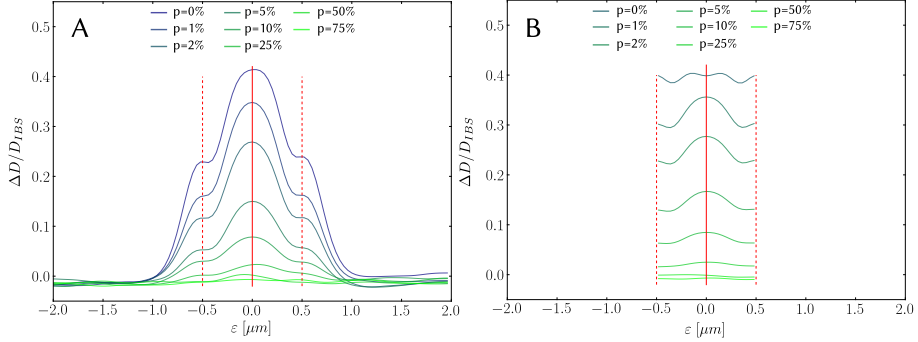


Figure 13 – (A) Average relative decrease in DC at various barrier permeabilities in the neighbourhood around a barrier for barriers placed 1 μm apart. ε indicates the distance of the center of the region used for DC estimation from the barrier. (B) Same as A except for barriers place 10 μm apart.

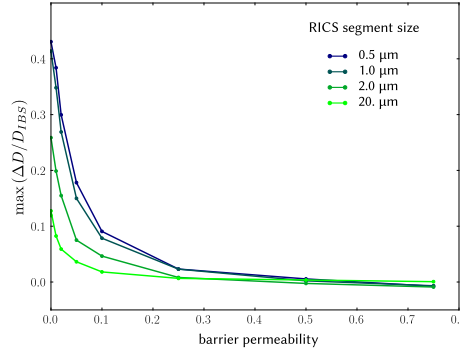


Figure 14 – Maximum relative decrease in DC as a function of barrier permeability. Different curves indicate analysis region lengths of 2,1 and 0.5 μm . The 20 μm region signifies analysis performed on the entire image.

reduced compared to all regional cases. Therefore, localized diffusion restrictions, represented here by barriers, result in more pronounced decreases in DCs when estimated on a smaller scale. On the large scale, however, this effect is lessened and appears as a uniform reduction in the apparent DC.

5.3 CONCLUSIONS

Applying RICS to 1D diffusion reveals that barriers affect estimation of DCs even if the area from which image data used for DC estimation was acquired does not contain a single barrier, but is nearby a region where a barrier is present. The distance at which this effect is observable depends on the permeability of the

barrier, the DC of the dye in the inter barrier space and the size of the segment used for apparent DC estimation.

6

HYPERTROPHIC CARDIOMYOPATHY IN RAF1 MUTANTS

NOONAN AND LEOPARD SYNDROMES are developmental disorders characterized by distinct facial features, chest deformities, short stature and a wide array of congenital heart diseases [2]. These diseases are linked to a variety of germline gain-of-function mutations. Mutations in serine/threonine-protein kinase (RAF1) have been determined to be the cause behind 3-5% of cases of Noonan and LEOPARD syndrome in affected individuals [20]. 90-95 % of patients with Noonan RAF1 mutations exhibit hypertrophic cardiomyopathy (HCM), whereas Noonan syndrome caused by mutations in other locations often lead to different cardiac defects. This suggests an important role for RAF1 in modulation of cardiac hypertrophy. RAF1 is a serine/theonine kinase which is part of a signalling pathway involved in transducing signals from the cell membrane to the nucleus. RAF1 regulation is intricate and is affected by protein-protein interactions, localization of the protein and phosphorylation at multiple residues. In Publication II the ability of RAF1 to regulate hypertrophy in cardiomyocytes was studied.

Three common RAF1 mutations were explored in order to determine whether and how these ultimately result in hypertrophy. It was established that two of the studied mutations, S257L and L613V, localized close to phosphorylation sites S259 and S621, promote HCM. The third mutation (D486N) was found not to cause HCM. Overexpression of wild-type RAF1 also stimulated hypertrophy. Treatment with cyclosporine-A (inhibitor of calcineurin) prevented both wild-type RAF1 and L613V induced HCM.

Wild-type RAF1 overexpression and L613V both result in dysregulation of Ca^{2+} signalling which was exemplified by spontaneous Ca^{2+} transients, slower decay rates and, in case of L613V, an increased sarcoplasmic reticulum Ca^{2+} load. This finding was attributed to down-regulation of sarco/endoplasmic reticulum Ca^{2+} ATPase (SERCA) through overexpression of wild-type and L613V RAF1.

The study conducted in Publication II established a link between HCM and arrhythmogenic Ca^{2+} dysregulation, found an interaction between calcineurin and RAF1, and identified a link for mutant RAF1 induced pathological HCM.

7

DEVELOPMENT OF CARDIAC ENERGETICS IN POSTNATAL MOUSE HEART

C OMPARTMENTATION OF ENERGY METABOLITES in cardiomyocytes aims to lessen the impact of abrupt changes in energy consumption and allows for high phosphorylation potential to exist where it is most required. Not much is known about the nature, structure and development of barriers responsible for such compartmentation. In the study reviewed in Publication I we summarize and comment on some of the aspects presented in a extensive investigation into how the structural and energetic properties of mouse heart muscle change during postnatal development [21].

The original paper concluded that energetic microdomains are formed very early in postnatal development and that the maturation of cellular architecture has an important role to play ensuring maximal flexibility in regulation of ATP production by mitochondria. Although an impressive amount of work had been invested by the authors of the original paper, we found several issues with the conclusions and questions left unanswered by the authors. We pointed out the misinterpretation of one derived variable used by the authors to propose an increase in the functional coupling between the adenine nucleotide translocase (ANT) and mitochondrial creatine kinase (CK). We proposed an alternative explanation of an increase in diffusion restrictions in the cytosol and suggested an experiment for measuring the coupling between ANT and mitochondrial CK. Furthermore, we used a different approach from the original authors to interpret their data and to focus on the changes of the role of energy supply pathways by eliminating auxiliary effects. We also suggested some possible directions for future research in this area. Namely, accounting for the changing role of glycolysis during maturation and employing computational models in analysing the data, which could help unravel the interplay between different factors during cell maturation.

8

CONCLUSIONS

THIS DISSERTATION EXPLORES VARIOUS aspects of cardiac function and dysfunction. The main conclusions deriving from this work are listed below, grouped according to the research topic.

EXTENDED RICS TECHNIQUE

- a) The extended RICS protocol developed during these doctoral studies is a useful tool for determining concentrations, diffusion coefficients and diffusional anisotropy of fluorescent dyes in cells.
- b) The RICS method, when applied to estimating diffusion in water, is able to reproduce the known DCs of the dye ATTO655-COOH with high accuracy.
- c) The “poking” technique is a good alternative to saponin permeabilization. It requires dedicated hardware in form of controllable micromanipulators and extra preparation in order to ensure cells remain on the coverslip after mechanical permeabilization. However in cases like anisotropic RICS measurements, where one protocol run can take several hours, good viability of cells is a necessity.
- d) Taking into account the possibility of fluorescent molecules entering into a triplet state enhanced the ability of the method to estimate DCs.
- e) Assuming two sub-species of the same dye to be diffusing in the cytosol, one slowly diffusing bound form and one freely diffusing form improved the results greatly when estimating DCs of ATTO633-ATP. In case of Alexa647-dextran 10K adding a second component was not necessary and did not improve fits to CF curves. This indicates that ATTO633-ATP is more actively binding to intracellular proteins or structures, whereas Alexa647-dextran 10K remains relatively inert.

CONCLUSIONS

ESTIMATION OF DIFFUSION COEFFICIENTS OF FLUORESCENT DYES

- f) Employing the RICS method, DCs of ATTO633-ATP were determined to be 326 ± 13 , 195 ± 8 , 24 ± 6 , $35 \pm 8 \mu\text{m}^2/\text{s}$ in water, artificial intracellular solution, transverse direction and longitudinal direction in the cardiomyocyte, respectively. Similarly, DCs of Alexa647-dextran 10K were determined to be 62 ± 1 , 53 ± 1 , 16 ± 2 , $19 \pm 3 \mu\text{m}^2/\text{s}$ in water, artificial intracellular solution, transverse direction and longitudinal direction in the cardiomyocyte, respectively.
- g) The relative decline in DCs when transitioning from solution to the intracellular environment was higher for ATTO633-ATP than for Alexa647-dextran 10K. Considering the fact that the molecular mass of ATTO633-ATP is ~ 9 times less than that of Alexa647-dextran 10K makes this result counterintuitive, whereby a smaller molecule is hindered more in the cytosol than the larger one.

MATHEMATICAL MODELLING OF RESTRICTED DIFFUSION

- h) The stochastic model of restricted diffusion with regular permeable barriers is able to reproduce the experimentally found DCs for ATTO633-ATP and Alexa647-dextran 10K when: barriers in the model are placed relatively close $< 1 \mu\text{m}$ apart, permeability of these barriers is low (containing $\sim 1 \dots 40$ pores of radius $7 \dots 30 \text{ nm per } \mu\text{m}^2$), diffusion coefficient in the inter barrier space is lower than diffusion in solution by a factor $0.8 \dots 1$.
- i) The model geometry used in this work is not the only one that is able to reproduce experimentally obtained DCs. Our choice was motivated by the relative simplicity of the employed geometry of the model.
- j) Computational experiments applying RICS to 1D diffusion reveal that barriers affect estimation of DCs even if the region used for estimation does not contain a barrier itself but is close to one. The distance at which this effect is observable depends on the permeability of the barrier, the DC of the dye in the inter barrier space and the size of the segment used for apparent DC estimation.

CARDIOMYOCYTE HYPERSTROPHY IN NOONAN SYNDROME

- k) The study conducted in Publication II established a link between hypertrophic cardiomyopathy (HCM) and overexpression or mutation of serine/threonine-protein kinase. Both wild-type and L613V RAF1 signal through calcineurin to induce hypertrophy in affected cardiomyocytes.

- l) RAF1 impairs calcium signalling by down-regulating SERCA but does not affect expression levels of other proteins involved in intracellular calcium signalling.
- m) Wild-type RAF1 overexpression and L613V both result in arrhythmogenic dysregulation of calcium signalling, indicated by spontaneous calcium transients during electrical stimulation, slower decay rates and, in case of L613V, an increased sarcoplasmic reticulum calcium load.
- n) Treatment with cyclosporine-A prevented both wild-type RAF1 and L613V induced HCM.

DEVELOPMENT OF ENERGETIC MICRODOMAINS

- o) Regeneration of energy metabolites through glycolysis is an important factor, especially during maturation, and should be included in the analysis of developmental changes in energy transfer pathways.
- p) Computational models could help interpret existing data and could reveal novel aspects of the interplay between various factors during cell maturation. Using statistical methods, different mathematical models could be compared to establish the existence of metabolite pools or compartmentation in the CM.

BIBLIOGRAPHY

BIBLIOGRAPHY

- [1] M. R. Abraham, V. Selivanov, D. Hodgson, D. Pucar, L. Zingman, B. Wieringa, P. Dzeja, A. Alekseev, and A. Terzic. Coupling of cell energetics with membrane metabolic sensing. *J. Biol. Chem.*, 277(27):24427 –24434, 2002.
- [2] J. E. Allanson. Noonan syndrome. *J. Med. Genet.*, 24(1):9, 1987.
- [3] C. M. Brown, R. B. Dalal, B. Hebert, M. A. Digman, A. R. Horwitz, and E. Gratton. Raster image correlation spectroscopy (rics) for measuring fast protein dynamics and concentrations with a commercial laser scanning confocal microscope. *J. Microsc.*, 229(1):78–91, 2008.
- [4] R. de Graaf, A. van Kranenburg, and K. Nicolay. In vivo 31p-nmr diffusion spectroscopy of atp and phosphocreatine in rat skeletal muscle. *Biophys. J.*, 78(4):1657–1664, 2000.
- [5] D. Del Re and J. Sadoshima. Is raf1 a nexus for cardiac hypertrophic signaling in human disease? *J. Mol. Cell. Cardiol.*, 51(1):1–3, 2011.
- [6] M. Digman, C. Brown, P. Sengupta, P. Wiseman, A. Horwitz, and E. Gratton. Measuring fast dynamics in solutions and cells with a laser scanning microscope. *Biophys. J.*, 89(2):1317–1327, 2005.
- [7] M. A. Digman and E. Gratton. Lessons in fluctuation correlation spectroscopy. *Annu Rev Phys Chem*, 62:645–668, 2011.
- [8] N. Gröner, J. Capoulade, C. Cremer, and M. Wachsmuth. Measuring and imaging diffusion with multiple scan speed image correlation spectroscopy. *Opt. Express*, 18(20):21225, 2010.
- [9] S. Gudbjarnason, P. Mathes, and K. G. Ravens. Functional compartmentation of atp and creatine phosphate in heart muscle. *J. Mol. Cell. Cardiol.*, 1(3):325–339, 1970.
- [10] E. Haustein and P. Schwille. Fluorescence correlation spectroscopy: novel variations of an established technique. *Annu. Rev. Biophys. Biomol. Struct.*, 36:151–169, 2007.

Bibliography

- [11] A. Kaasik, V. Veksler, E. Boehm, M. Novotova, A. Minajeva, and R. Ventura-Clapier. Energetic crosstalk between organelles: Architectural integration of energy production and utilization. *Circ. Res.*, 89(2):153–159, 2001.
- [12] O. Krichevsky and G. Bonnet. Fluorescence correlation spectroscopy: the technique and its applications. *Reports on Prog. Phys.*, 65(2):251, 2002.
- [13] L. Kümmel. Ca_{mg}-atpase activity of permeabilized rat heart cells and its functional coupling to oxidative phosphorylation of the cells. *Cardiovasc. Res.*, 22:359–367, 1988.
- [14] F. T. Kurz, M. A. Aon, B. O’Rourke, and A. A. Armoundas. Spatio-temporal oscillations of individual mitochondria in cardiac myocytes reveal modulation of synchronized mitochondrial clusters. *Proc. Natl. Acad. Sci.*, 107(32):14315, 2010.
- [15] M. J. Kushmerick and R. J. Podolsky. Ionic mobility in muscle cells. *Science (80-)*, 166(910):1297–1298, 1969.
- [16] J. Lakowicz. *Principles of fluorescence spectroscopy*. Springer, 2006.
- [17] C. B. Müller, A. Loman, V. Pacheco, F. Koberling, D. Willbold, W. Richtering, and J. Enderlein. Precise measurement of diffusion by multi-color dual-focus fluorescence correlation spectroscopy. *EPL (Europhysics Letters)*, 83:46001, 2008.
- [18] N. Muramatsu and A. Minton. Tracer diffusion of globular proteins in concentrated protein solutions. *Proc. Natl. Acad. Sci.*, 85(9):2984 –2988, 1988.
- [19] S. Neubauer. The failing heart—an engine out of fuel. *N. Engl. J. Med.*, 356(11):1140–1151, 2007.
- [20] B. Pandit, A. Sarkozy, L. A. Pennacchio, C. Carta, K. Oishi, S. Martinelli, E. A. Pogna, W. Schackwitz, A. Ustaszewska, A. Landstrom, and Others. Gain-of-function raf1 mutations cause noonan and leopard syndromes with hypertrophic cardiomyopathy. *Nat. Genet.*, 39(8):1007–1012, 2007.
- [21] J. Piquereau, M. Novotova, D. Fortin, A. Garnier, R. Ventura-Clapier, V. Veksler, and F. Joubert. Postnatal development of mouse heart: formation of energetic microdomains. *J. Physiol. (Lond.)*, 588(13):2443–2454, 2010.
- [22] H. Ramay, O. Liu, and E. Sobie. Recovery of cardiac calcium release is controlled by sarcoplasmic reticulum refilling and ryanodine receptor sensitivity. *Cardiovasc. Res.*, 91(4):598 –605, 2011.

- [23] H. Ramay and M. Vendelin. Diffusion restrictions surrounding mitochondria: A mathematical model of heart muscle fibers. *Biophys. J.*, 97(2):443–452, 2009.
- [24] V. Saks, A. Kuznetsov, T. Andrienko, Y. Usson, F. Appaix, K. Guerrero, T. Kaambre, P. Sikk, M. Lemba, and M. Vendelin. Heterogeneity of ADP diffusion and regulation of respiration in cardiac cells. *Biophys. J.*, 84(5):3436–3456, 2003.
- [25] M. Sepp, M. Vendelin, H. Vija, and R. Birkedal. ADP compartmentation analysis reveals coupling between pyruvate kinase and ATPases in heart muscle. *Biophys. J.*, 98(12):2785–2793, 2010.
- [26] P. Shorten and J. Sneyd. A mathematical analysis of obstructed diffusion within skeletal muscle. *Biophys. J.*, 96(12):4764–4778, 2009.
- [27] M. Tartaglia, L. A. Pennacchio, C. Zhao, K. K. Yadav, V. Fodale, A. Sarkozy, B. Pandit, K. Oishi, S. Martinelli, W. Schackwitz, and Others. Gain-of-function sos1 mutations cause a distinctive form of noonan syndrome. *Nat. Genet.*, 39(1):75–79, 2006.
- [28] Nancy Thompson. Fluorescence correlation spectroscopy. In Joseph Lakowicz, Chris D. Geddes, and Joseph R. Lakowicz, editors, *Topics in Fluorescence Spectroscopy*, volume 1 of *Topics in Fluorescence Spectroscopy*, pages 337–378. Springer US, 2002.
- [29] M. Vendelin and R. Birkedal. Anisotropic diffusion of fluorescently labeled atp in rat cardiomyocytes determined by raster image correlation spectroscopy. *Am. J. Physiol. Cell. Physiol.*, 295(5):C1302–1315, 2008.
- [30] M. Vendelin, M. Eimre, E. Seppet, N. Peet, T. Andrienko, M. Lemba, J. Engelbrecht, E. Seppet, and V. Saks. Intracellular diffusion of adenosine phosphates is locally restricted in cardiac muscle. *Mol. Cell. Biochem.*, 256(1/2):229–241, 2004.
- [31] J. Widengren, U. Mets, and R. Rigler. Fluorescence correlation spectroscopy of triplet states in solution: a theoretical and experimental study. *J Phys Chem*, 99(36):13368–13379, 1995.

CURRICULUM VITAE

Curriculum Vitae

Replace **papers/cv_eng.pdf** with the pdf of
your own English CV

Elulookirjeldus

Replace **papers/cv_est.pdf** with the pdf of
your own Estonian CV

APPENDIX

PUBLICATION I

Illaste A, Kalda M, Schryer DW, Sepp M

Life of mice - development of cardiac energetics.

Journal of Physiology, 588(23), December 2010

Replace **papers/paperI.pdf** with the pdf of
your own paper I

PUBLICATION II

Dhandapani P, Fabris F, Tonk R, Illaste A, Karakikes I, Sorourian M, Sheng J, Hajjar R, Tartaglia M, Sobie R, Lebeche D, Gelb B

Cyclosporine attenuates cardiomyocyte hypertrophy induced by RAF1 mutants in Noonan and LEOPARD syndromes.

Journal of Molecular and Cellular Cardiology, Volume 51, Issue 1, July 2011

Replace **papers/paperII.pdf** with the pdf of
your own paper II

PUBLICATION III

Illaste A, Laasmaa M, Peterson P, Vendelin M

Analysis of molecular movement reveals latticelike obstructions to diffusion in heart muscle cells.

Biophysical Journal, 2012, *in press*

Replace **papers/paperIII.pdf** with the pdf of
your own paper III

DISSSERTATIONS DEFENDED
AT TALLINN UNIVERSITY OF TECHNOLOGY
ON NATURAL AND EXACT SCIENCES

1. **Olav Kongas.** *Nonlinear Dynamics in Modeling Cardiac Arrhythmias.* 1998.
2. **Kalju Vanatalu.** *Optimization of Processes of Microbial Biosynthesis of Isotopically Labeled Biomolecules and Their Complexes.* 1999.
3. **Ahto Buldas.** *An Algebraic Approach to the Structure of Graphs.* 1999.
4. **Monika Drews.** *A Metabolic Study of Insect Cells in Batch and Continuous Culture: Application of Chemostat and Turbidostat to the Production of Recombinant Proteins.* 1999.
5. **Eola Valdre.** *Endothelial-Specific Regulation of Vessel Formation: Role of Receptor Tyrosine Kinases.* 2000.
6. **Kalju Lott.** *Doping and Defect Thermodynamic Equilibrium in ZnS.* 2000.
7. **Reet Koljak.** *Novel Fatty Acid Dioxygenases from the Corals *Plexaura homomalla* and *Gersemia fruticosa*.* 2001.
8. **Anne Paju.** *Asymmetric oxidation of Prochiral and Racemic Ketones by Using Sharpless Catalyst.* 2001.
9. **Marko Vendelin.** *Cardiac Mechanoenetics in silico.* 2001.
10. **Pearu Peterson.** *Multi-Soliton Interactions and the Inverse Problem of Wave Crest.* 2001.
11. **Anne Menert.** *Microcalorimetry of Anaerobic Digestion.* 2001.
12. **Toomas Tiivel.** *The Role of the Mitochondrial Outer Membrane in in vivo Regulation of Respiration in Normal Heart and Skeletal Muscle Cell.* 2002.
13. **Olle Hints.** *Ordovician Scolecodonts of Estonia and Neighbouring Areas: Taxonomy, Distribution, Palaeoecology, and Application.* 2002.
14. **Jaak Nõlvak.** *Chitinozoan Biostratigraphy in the Ordovician of Baltoscandia.* 2002.
15. **Liivi Kluge.** *On Algebraic Structure of Pre-Operad.* 2002.
16. **Jaanus Lass.** *Biosignal Interpretation: Study of Cardiac Arrhythmias and Electromagnetic Field Effects on Human Nervous System.* 2002.
17. **Janek Peterson.** *Synthesis, Structural Characterization and Modification of PAMAM Dendrimers.* 2002.
18. **Merike Vaher.** *Room Temperature Ionic Liquids as Background Electrolyte Additives in Capillary Electrophoresis.* 2002.
19. **Valdek Mikli.** *Electron Microscopy and Image Analysis Study of Powdered Hardmetal Materials and Optoelectronic Thin Films.* 2003.
20. **Mart Viljus.** *The Microstructure and Properties of Fine-Grained Cermets.* 2003.
21. **Signe Kask.** *Identification and Characterization of Dairy-Related Lactobacillus.* 2003
22. **Tiiu-Mai Laht.** *Influence of Microstructure of the Curd on Enzymatic and Microbiological Processes in Swiss-Type Cheese.* 2003.
23. **Anne Kuuskosalu.** *2-5A Synthetase in the Marine Sponge *Geodia cydonium*.* 2003.
24. **Sergei Bereznev.** *Solar Cells Based on Polycrystalline Copper-Indium Chalcogenides and Conductive Polymers.* 2003.
25. **Kadri Kriis.** *Asymmetric Synthesis of C₂-Symmetric Bimorpholines and Their Application as Chiral Ligands in the Transfer Hydrogenation of Aromatic Ketones.* 2004.
26. **Jekaterina Reut.** *Polypyrrole Coatings on Conducting and Insulating Substrates.* 2004.
27. **Sven Nõmm.** *Realization and Identification of Discrete-Time Nonlinear Systems.* 2004.
28. **Olga Kijatkina.** *Deposition of Copper Indium Disulphide Films by Chemical Spray Pyrolysis.* 2004.
29. **Gert Tamberg.** *On Sampling Operators Defined by Rogosinski, Hann and Blackman Windows.* 2004.
30. **Monika Übner.** *Interaction of Humic Substances with Metal Cations.* 2004.
31. **Kaarel Adamberg.** *Growth Characteristics of Non-Starter Lactic Acid Bacteria from Cheese.* 2004.
32. **Imre Vallikivi.** *Lipase-Catalysed Reactions of Prostaglandins.* 2004.
33. **Merike Peld.** *Substituted Apatites as Sorbents for Heavy Metals.* 2005.
34. **Vitali Syritski.** *Study of Synthesis and Redox Switching of Polypyrrole and Poly(3,4-ethylenedioxythiophene) by Using in-situ Techniques.* 2004.
35. **Lee Pöllumaa.** *Evaluation of Ecotoxicological Effects Related to Oil Shale Industry.* 2004.
36. **Riina Aav.** *Synthesis of 9,11-Secosterols Intermediates.* 2005.
37. **Andres Braunbrück.** *Wave Interaction in Weakly Inhomogeneous Materials.* 2005.

Publication III

38. **Robert Kitt.** *Generalised Scale-Invariance in Financial Time Series.* 2005.
39. **Juss Pavelson.** *Mesoscale Physical Processes and the Related Impact on the Summer Nutrient Fields and Phytoplankton Blooms in the Western Gulf of Finland.* 2005.
40. **Olari Ilison.** *Solitons and Solitary Waves in Media with Higher Order Dispersive and Nonlinear Effects.* 2005.
41. **Maksim Säkki.** *Intermittency and Long-Range Structurization of Heart Rate.* 2005.
42. **Enli Kiipli.** *Modelling Seawater Chemistry of the East Baltic Basin in the Late Ordovician–Early Silurian.* 2005.
43. **Igor Golovtsov.** *Modification of Conductive Properties and Processability of Polyparaphenylene, Polyppyrrole and polyaniline.* 2005.
44. **Katrin Laos.** *Interaction Between Furcellaran and the Globular Proteins (Bovine Serum Albumin β -Lactoglobulin).* 2005.
45. **Arvo Mere.** *Structural and Electrical Properties of Spray Deposited Copper Indium Disulphide Films for Solar Cells.* 2006.
46. **Sille Ehala.** *Development and Application of Various On- and Off-Line Analytical Methods for the Analysis of Bioactive Compounds.* 2006.
47. **Maria Kulp.** *Capillary Electrophoretic Monitoring of Biochemical Reaction Kinetics.* 2006.
48. **Anu Aaspöllu.** *Proteinases from Vipera lebetina Snake Venom Affecting Hemostasis.* 2006.
49. **Lyudmila Chekulayeva.** *Photosensitized Inactivation of Tumor Cells by Porphyrins and Chlorins.* 2006.
50. **Merle Uudsemaa.** *Quantum-Chemical Modeling of Solvated First Row Transition Metal Ions.* 2006.
51. **Tagli Pitsi.** *Nutrition Situation of Pre-School Children in Estonia from 1995 to 2004.* 2006.
52. **Angela Ivask.** *Luminescent Recombinant Sensor Bacteria for the Analysis of Bioavailable Heavy Metals.* 2006.
53. **Tiina Lõugas.** *Study on Physico-Chemical Properties and Some Bioactive Compounds of Sea Buckthorn (*Hippophae rhamnoides* L.).* 2006.
54. **Kaja Kasemets.** *Effect of Changing Environmental Conditions on the Fermentative Growth of *Saccharomyces cerevisiae* S288C: Auxo-accelerostat Study.* 2006.
55. **Ildar Nisamedtinov.** *Application of ^{13}C and Fluorescence Labeling in Metabolic Studies of *Saccharomyces spp.** 2006.
56. **Alar Leibak.** *On Additive Generalisation of Voronoi's Theory of Perfect Forms over Algebraic Number Fields.* 2006.
57. **Andri Jagomägi.** *Photoluminescence of Chalcopyrite Tellurides.* 2006.
58. **Tõnu Martma.** *Application of Carbon Isotopes to the Study of the Ordovician and Silurian of the Baltic.* 2006.
59. **Marit Kauk.** *Chemical Composition of CuInSe₂ Monograins Powders for Solar Cell Application.* 2006.
60. **Julia Kois.** *Electrochemical Deposition of CuInSe₂ Thin Films for Photovoltaic Applications.* 2006.
61. **Ilona Oja Açık.** *Sol-Gel Deposition of Titanium Dioxide Films.* 2007.
62. **Tiiia Anmann.** *Integrated and Organized Cellular Bioenergetic Systems in Heart and Brain.* 2007.
63. **Katrin Trummal.** *Purification, Characterization and Specificity Studies of Metalloproteinases from Vipera lebetina Snake Venom.* 2007.
64. **Gennadi Lessin.** *Biochemical Definition of Coastal Zone Using Numerical Modeling and Measurement Data.* 2007.
65. **Enno Pais.** *Inverse problems to determine non-homogeneous degenerate memory kernels in heat flow.* 2007.
66. **Maria Borissova.** *Capillary Electrophoresis on Alkylimidazolium Salts.* 2007.
67. **Karin Valmsen.** *Prostaglandin Synthesis in the Coral *Plexaura homomalla*: Control of Prostaglandin Stereochemistry at Carbon 15 by Cyclooxygenases.* 2007.
68. **Kristjan Piirimäe.** *Long-Term Changes of Nutrient Fluxes in the Drainage Basin of the Gulf of Finland – Application of the PolFlow Model.* 2007.
69. **Tatjana Dedova.** *Chemical Spray Pyrolysis Deposition of Zinc Sulfide Thin Films and Zinc Oxide Nanostructured Layers.* 2007.
70. **Katrin Tomson.** *Production of Labelled Recombinant Proteins in Fed-Batch Systems in *Escherichia coli*.* 2007.
71. **Cecilia Sarmiento.** *Suppressors of RNA Silencing in Plants.* 2008.
72. **Vilja Mardla.** *Inhibition of Platelet Aggregation with Combination of Antiplatelet Agents.* 2008.
73. **Maie Bachmann.** *Effect of Modulated Microwave Radiation on Human Resting Electroencephalographic Signal.* 2008.
74. **Dan Hüvonen.** *Terahertz Spectroscopy of Low-Dimensional Spin Systems.* 2008.
75. **Ly Villo.** *Stereoselective Chemoenzymatic Synthesis of Deoxy Sugar Esters Involving *Candida antarctica* Lipase B.* 2008.

Publication III

76. **Johan Anton.** *Technology of Integrated Photoelasticity for Residual Stress Measurement in Glass Articles of Axisymmetric Shape.* 2008.
77. **Olga Volobujeva.** *SEM Study of Selenization of Different Thin Metallic Films.* 2008.
78. **Artur Jõgi.** *Synthesis of 4'-Substituted 2,3'-dideoxynucleoside Analogues.* 2008.
79. **Mario Kadastik.** *Doubly Charged Higgs Boson Decays and Implications on Neutrino Physics.* 2008.
80. **Fernando Pérez-Caballero.** *Carbon Aerogels from 5-Methylresorcinol-Formaldehyde Gels.* 2008.
81. **Sirje Vaask.** *The Comparability, Reproducibility and Validity of Estonian Food Consumption Surveys.* 2008.
82. **Anna Menaker.** *Electrosynthesized Conducting Polymers, Polypyrrole and Poly(3,4-ethylenedioxythiophene), for Molecular Imprinting.* 2009.
83. **Lauri Ilison.** *Solitons and Solitary Waves in Hierarchical Korteweg-de Vries Type Systems.* 2009.
84. **Kaia Ernits.** *Study of In₂S₃ and ZnS Thin Films Deposited by Ultrasonic Spray Pyrolysis and Chemical Deposition.* 2009.
85. **Veljo Sinivee.** *Portable Spectrometer for Ionizing Radiation “Gammamapper”.* 2009.
86. **Jüri Virkepu.** *On Lagrange Formalism for Lie Theory and Operadic Harmonic Oscillator in Low Dimensions.* 2009.
87. **Marko Piirsoo.** *Deciphering Molecular Basis of Schwann Cell Development.* 2009.
88. **Kati Helmja.** *Determination of Phenolic Compounds and Their Antioxidative Capability in Plant Extracts.* 2010.
89. **Merike Sömera.** *Sobemoviruses: Genomic Organization, Potential for Recombination and Necessity of P1 in Systemic Infection.* 2010.
90. **Kristjan Laes.** *Preparation and Impedance Spectroscopy of Hybrid Structures Based on CuIn₃Se₅ Photoabsorber.* 2010.
91. **Kristin Lippur.** *Asymmetric Synthesis of 2,2'-Bimorpholine and its 5,5'-Substituted Derivatives.* 2010.
92. **Merike Luman.** *Dialysis Dose and Nutrition Assessment by an Optical Method.* 2010.
93. **Mikhail Berezovski.** *Numerical Simulation of Wave Propagation in Heterogeneous and Microstructured Materials.* 2010.
94. **Tamara Aid-Pavlidis.** *Structure and Regulation of BDNF Gene.* 2010.
95. **Olga Bragina.** *The Role of Sonic Hedgehog Pathway in Neuro- and Tumorigenesis.* 2010.
96. **Merle Randriüt.** *Wave Propagation in Microstructured Solids: Solitary and Periodic Waves.* 2010.
97. **Marju Laars.** *Asymmetric Organocatalytic Michael and Aldol Reactions Mediated by Cyclic Amines.* 2010.
98. **Maarja Grossberg.** *Optical Properties of Multinary Semiconductor Compounds for Photovoltaic Applications.* 2010.
99. **Alla Maloverjan.** *Vertebrate Homologues of Drosophila Fused Kinase and Their Role in Sonic Hedgehog Signalling Pathway.* 2010.
100. **Priit Pruunsild.** *Neuronal Activity-Dependent Transcription Factors and Regulation of Human BDNF Gene.* 2010.
101. **Tatjana Knjazeva.** *New Approaches in Capillary Electrophoresis for Separation and Study of Proteins.* 2011.
102. **Atanas Katerski.** *Chemical Composition of Sprayed Copper Indium Disulfide Films for Nanostructured Solar Cells.* 2011.
103. **Kristi Timmo.** *Formation of Properties of CuInSe₂ and Cu₂ZnSn(S,Se)₄ Monograins Powders Synthesized in Molten KL.* 2011.
104. **Kert Tamm.** *Wave Propagation and Interaction in Mindlin-Type Microstructured Solids: Numerical Simulation.* 2011.
105. **Adrian Popp.** *Ordovician Proetid Trilobites in Baltoscandia and Germany.* 2011.
106. **Ove Pärn.** *Sea Ice Deformation Events in the Gulf of Finland and This Impact on Shipping.* 2011.
107. **Germo Väli.** *Numerical Experiments on Matter Transport in the Baltic Sea.* 2011.
108. **Andrus Seiman.** *Point-of-Care Analyser Based on Capillary Electrophoresis.* 2011.
109. **Olga Katargina.** *Tick-Borne Pathogens Circulating in Estonia (Tick-Borne Encephalitis Virus, Anaplasma phagocytophilum, Babesia Species): Their Prevalence and Genetic Characterization.* 2011.
110. **Ingrid Sumeri.** *The Study of Probiotic Bacteria in Human Gastrointestinal Tract Simulator.* 2011.
111. **Kairit Zovo.** *Functional Characterization of Cellular Copper Proteome.* 2011.
112. **Natalja Makarytsheva.** *Analysis of Organic Species in Sediments and Soil by High Performance Separation Methods.* 2011.
113. **Monika Mortimer.** *Evaluation of the Biological Effects of Engineered Nanoparticles on Unicellular Pro- and Eukaryotic Organisms.* 2011.

Publication III

114. **Kersti Tepp.** *Molecular System Bioenergetics of Cardiac Cells: Quantitative Analysis of Structure-Function Relationship.* 2011.
115. **Anna-Liisa Peikolainen.** *Organic Aerogels Based on 5-Methylresorcinol.* 2011.
116. **Leeli Amon.** *Palaeoecological Reconstruction of Late-Glacial Vegetation Dynamics in Eastern Baltic Area: A View Based on Plant Macrofossil Analysis.* 2011.
117. **Tanel Peets.** *Dispersion Analysis of Wave Motion in Microstructured Solids.* 2011.
118. **Liina Kaupmees.** *Selenization of Molybdenum as Contact Material in Solar Cells.* 2011.
119. **Allan Olspern.** *Properties of VPg and Coat Protein of Sobemoviruses.* 2011.
120. **Kadri Koppel.** *Food Category Appraisal Using Sensory Methods.* 2011.
121. **Jelena Gorbatšova.** *Development of Methods for CE Analysis of Plant Phenolics and Vitamins.* 2011.
122. **Karin Viipsi.** *Impact of EDTA and Humic Substances on the Removal of Cd and Zn from Aqueous Solutions by Apatite.* 2012.
123. **David W. Schryer.** *Metabolic Flux Analysis of Compartmentalized Systems using Dynamic Isotopologue Modeling.* 2012